N96-17706

MODELING AND CHARACTERIZATION OF THROUGH-THE-THICKNESS PROPERTIES OF 3D WOVEN COMPOSITES

Dru Hartranft, Azar Pravizi-Majidi and Tsu-Wei Chou
Center for Composite Materials
University of Delaware
Newark, DE

SUMMARY

The through-the-thickness properties of three-dimensionally (3D) woven carbon/epoxy composites have been studied. The investigation aimed at the evaluation and development of test methodologies for the property characterization in the thickness direction, and the establishment of fiber architecture-property relationships in woven textile structural composites. Three woven architectures were studied: layer-to-layer Angle Interlock, through-the-thickness Angle Interlock, and through-the-thickness Orthogonal. A through-the-thickness Orthogonal woven preform with surface pile was also designed and manufactured for the fabrication of tensile test coupons with integrated grips. All the preforms were infiltrated by the resin transfer molding technique. The microstructures of the composites were characterized along the warp and fill (weft) directions to determine the degree of yarn undulations, yarn cross-sectional shapes, and micro-structural dimensions. These parameters were correlated to the fiber architecture. Specimens were designed and tested for the direct measurement of the through-the-thickness tensile, compressive and shear properties of the composites. Design optimization was conducted through the analysis of the stress fields within the specimen coupled with experimental verification. The experimentally-derived elastic properties in the thickness direction compared well with analytical predictions obtained from a volume averaging model .

INTRODUCTION

Woven and braided composite materials have been the subject of a great deal of research due to the superior through-the-thickness properties and delamination resistance over laminated composites, and the potential for near net shape processing. Numerous predictive models exist for the in-plane and through-the-thickness thermo-elastic properties of braided and woven textile composites. [1-5] Experimental validation of these models has been performed for in-plane properties and good agreement has been observed. However, very limited experimental work has been conducted for through-the-thickness properties due to the difficulty of such experiments and the lack of suitable test methods. The small out-of-plane dimensions of textile composite panels makes the introduction of a uniform tensile, compressive or shear stress field extremely difficult, if not impossible.

This work summarizes the results of an effort by the investigators to study testing and mechanical behavior of 3D woven polymer matrix composites in the thickness direction. The work reported here covers through-the-thickness tension, through-the-thickness compression, interlaminar shear, and transverse (i.e., through-the-thickness) shear testing. In addition, Mode I interlaminar fracture toughness behavior of the composites was also evaluated and the results will be presented in a separate report.

PRECEDING PAGE BLANK NOT FILMED

MATERIAL DESCRIPTION

Table 1 summarizes the architectures, thicknesses and tow sizes of the composites used in this investigation. The composites utilized Hercules AS-4 fibers and Shell 1895 epoxy resin. The 3D woven composites had layer-to-layer angle interlock (the LS series), through-the-thickness angle interlock (the TS series), and through-the-thickness orthogonal (the OS series) architectures. The 0.25" thick panels were used for interlaminar shear tests and Mode I interlaminar fracture toughness tests. The 1" thick panels were utilized in the through-the-thickness tensile, compressive and shear tests. All the preforms were woven by Textile Technologies, Inc. (TTI) of Hatboro, Pa. and impregnated by resin transfer molding (RTM) at Boeing of Seattle, WA. In addition to the above materials, a special orthogonal woven composite, the OS-4 panel, was designed and fabricated for through-the-thickness tension testing. This composite had an architecture similar to that of OS-3 except that it contained surface fiber tows attached to the first layer of the warp stuffer tows, forming a 1" long pile on each surface. The surface pile provided for the design of an integrated-grip specimen. The OS-4 panel was impregnated by the investigators using a especially designed mold and RTM processing. Schematics of the layer-to-layer angle interlock, through-the-thickness angle interlock, and orthogonal woven architectures are shown in Figures 1 through 3, respectively. Throughout this work the axes x, y, and z refer to the warp, weft, and thickness directions of the woven composite panels.

Prior to the characterization of the mechanical properties, the fiber volume fraction and microstructure of each panel were determined. This information was required for elastic property modeling. Fiber volume fractions were measured from a minimum of three samples taken from random locations in the panels. Overall fiber volume fractions and void volume fractions were determined using the acid digestion method (ASTM-3171 standard). Directional fiber volume fractions were measured from polished cross sections perpendicular to the warp and weft directions of panels by means of image analysis using NIH 1.54 image analysis software. A summary of the overall and directional fiber volume fractions of each panel is presented in Table 2.

The weave architecture controls the elastic and strength properties of the composite. The repeat structure of the 3D woven materials represents the warp weaver pattern and the weft stacking sequence. Two repeat units are often used to describe the structures of 3D woven materials. A "unit cell" is defined as the smallest segment of the architecture which can be equivalently translated in any direction. This cell does not, however, include the interlacings and surface tow weavers. Therefore, in order to describe the entire structure, a "macro-cell" has been defined. The macro-cell includes the entire thickness thus capturing any surface weavers, as well as the entire weave shifting sequence along the weft tows. Figure 4 illustrates the unit cell and macro-cell for a layer-to-layer angle interlock architecture. The microstructure of each panel was analyzed by microscopy of cross sections perpendicular to the warp and weft directions. Tow sizes and shapes were noted and measured and used to determine the dimensions of the unit cells and macro-cells of each architecture. Tow sizes were measured using NIH 1.54 image analysis software. A summary of the unit-cell and macro-cell dimensions of each composite is presented in Tables 3 and 4, respectively.

In addition to characterizing the dimensions of the repeat structures of each composite, the investigation also revealed the effects of processing on the composite micro structure. The high volume fractions (minimum 60%) desired for the parts requires compacting the dry preforms. The compacting causes distortion of the preform architecture, therefore affecting the composite properties. Several examples of the resulting warp weaver tow distortion for the 1" thick panels are presented in Figure 5. As the figures show, the distortion is quite severe and will obviously have a dramatic effect on the properties of the composite. The effects of the tow distortion on mechanical properties will be discussed in subsequent sections.

ORIGINAL PAGE IS
OF POOR QUALITY

ELASTIC PROPERTY MODELING

Numerous schemes have been developed to estimate the thermo-elastic properties of 3D woven and braided materials. Some examples of these models include Yang, Ma and Chou's fiber inclination model [4]; Byun, Du and Chou's macro-cell model [1]; and a modified version of the macro-cell model, which includes more stringent cell boundary conditions, proposed by Pochiraju, Chou and Majidi [8] . These models use micromechanical predictions of tow properties followed by volume averaging of translated tow properties based on tow positions in the unit or macro-cell.

In order to predict the elastic properties of composites used in this work, the macro-cell model of Pochiraju et al. was modified to include the effect of distorted warp weaver tows. These properties were required for the design of the through-the-thickness tensile and compressive specimens, as well as the verification of the experimental results.

The RTM-induced tow distortion was modeled using a simplified sinusoidal path approximation (see Figure 6). The wavelength, λ, of the approximated sinusoidal was determined from the weave parameters of the architecture and the unit or macro-cell dimensions. The amplitude of the path was approximated using fiber volume fraction data, the weave parameters of the composite and macro-cell dimensions. First, the length of each warp weaver tow was determined using Equation (1).

$$L = \frac{4VV_{fz}}{tcz\,N_z\,\pi\,d_f^2} \qquad (1)$$

Where L is the length of the warp weaver tow, V is the volume of the macro-cell, V_{fz} is the volume fraction of warp weaver tows, tcz is the number of carbon fibers in a warp weaver tow, N_z is the number of warp weaver tows in the macro-cell, and d_f is the diameter of a carbon fiber. The length of each warp weaver tow in the macro cell is then used with the following equation to determine A, the amplitude of the distorted tow

$$L = \int_0^{Lzi} \sqrt{1 + \left(\frac{2\pi A}{\lambda} cos\left(\frac{2\pi x'}{\lambda}\right)\right)^2}\, dx' \qquad (2)$$

Where L_{zi} is the straight line distance between warp weaver interlacings, and the x' axis is oriented along the ideal path of the warp weaver tow (Figure 6). The L value from Equation (1) and the calculated value of λ allow the amplitude A to be solved for using an iterative scheme.

After the amplitude of the distorted tow was determined, the micro mechanical properties of the tow were calculated by averaging along the path of the tow, assuming iso-strain condition. The warp weaver, as well as the warp stuffer and weft tows, were assumed to be transversely isotropic bodies with axial and transverse elastic properties determined from the upper and lower bound rule of mixture approximations, respectively. The upper and lower bound approximations of the engineering constants of the warp weaver tow were then assembled into a stiffness matrix following equations presented in [9]. The overall properties of the distorted warp weaver tows were then averaged over the path of undulation by Equation (3)

$$C'_{ij} = \frac{1}{Lzi}\int_0^{Lzi}[T][C][T]^T dx' \qquad (3)$$

Where C'_{ij}'s are the components of the stiffness matrix of the warp weaver tow in the x' y' coordinate system in Figure 6 and [T] is the standard transformation matrix about the z' axis. This matrix can also be found in [9]. This averaging scheme was carried out numerically. The orientation angle along the undulating tow which is used in the [T] matrix is obtained from the slope of the tow by Equation (4)

$$\theta = tan^{-1}\left(\frac{2A\pi}{\lambda}cos\left(\frac{2\pi x'}{\lambda}\right)\right) \qquad (4)$$

Following the averaging scheme of Equation (3), the micro mechanical properties of the distorted tow are transformed to the coordinate system of the composite panel (the x y system in Figure 6) and used in the volume averaging scheme described in [8]. A summary of the predicted elastic properties using the above micro mechanical model and Pochiraju et al's modified macro-cell model is presented in Table 5.

THROUGH-THE-THICKNESS TENSILE TESTING

Specimen Design

A parallel-sided, multi-section specimen consisting of a test section and transition sections was designed for direct through-the-thickness tensile testing. Shan, Majidi, and Chou [7] conducted a detailed 2D stress analysis of the specimen using Boundary Element Analysis (BEA) method in order to optimize the specimen dimensions and reduce stress singularity at the test section/transition section interface. This singularity followed the forms shown in Equations (5) and (6) for displacements and stresses respectively.

$$u_i \propto r^{1-\alpha} \qquad (5)$$

$$\sigma_{ij} \propto r^{-\alpha} \qquad (6)$$

The BEA showed that α was a function of the specimen geometry and the elastic properties of the test and transition sections. The BEA also showed that α became zero for isotropic and orthotropic materials when:

$$\left(\frac{\nu_{ij}}{G_{ij}}\right)_{test} = \left(\frac{\nu_{ij}}{G_{ij}}\right)_{transition} \qquad (7)$$

Therefore, the transition sections must have Poisson's ratio/shear modulus ratio that closely matched that of the test section. Material selection for the transition sections therefore requires reliable predictions of the elastic properties of the composite to be tested.

Besides the dimensional optimizations and property matching, the BEA also showed that notching the transition section above the interface would further reduce α. Figures 7 and 8 show the notched and un-notched bi-material specimens with optimized dimensions, respectively.

Two approaches were followed for the introduction of the transition sections. In the first approach, the transition sections were adhesively bonded to the test section. This specimen configuration was designated the "bi-material specimen" and could be used only for the determination of the elastic properties due to the early failure of the bonded joint. In an effort to delay failure in order to examine the entire stress-strain response, and perhaps obtain the through-the-thickness strength, a second specimen configuration, designated the "integrated-grip specimen" was designed using the OS-4 preform architecture shown in Figure 3a. The surface piles in the OS-4 preform provided for transition sections that were integrally woven to the test section, thus avoiding bonded interfaces in the specimen. Details of the fabrication and testing of the bi-material and integrated-grip specimens are described below.

Specimen fabrication and Testing Procedures

The Bi-Material Specimen Configuration

In order to assess the validity of the bi-material specimen design, three specimen configurations were produced with a TS-3 test section. The first configuration, denoted generation 1, did not use the optimal specimen dimensions or transition/test section material matching. The second specimen configuration, denoted generation 2 (see Figure 7), utilized the optimized specimen geometry and material matching, but did not utilize notches above the interface. The last specimen configuration, denoted generation 3 (see Figure 8), was identical to the generation 2 specimen but utilized notches above the interface as described in the previous section. Only generation 3 specimen was used for tests on LS-3 and OS-3 panels.

The transition sections were 2D glass fabric reinforced epoxy composites fabricated by RTM processing using Shell Epon 862 epoxy resin. The glass fabrics used and their composite properties are shown in Table 6 [10]. These were selected to provide good matching with the predicted elastic properties of Table 5 for the 1" thick (i.e., LS-3, TS-3, and OS-3) woven composites. Table 7 presents the proposed transition and test section combinations for the measurement of E_{33}, ν_{23} and ν_{13} and the predicted α at the corner of the transition section/test section interface.

The test section and transition sections were cut to the proper dimensions and bonded together with American Cyanamid FM-300 film adhesive using a especially designed bonding fixture. The bonding fixture was utilized to assure that constant bonding pressure and specimen alignment were maintained during the cure cycle.

Specimens were cut and prepared along both orientations (i.e., with their wide surfaces parallel to warp or weft directions) in order to measure E_{33} and both ν_{23} and ν_{13}. Electrical resistance strain gages were affixed to both surfaces of each specimen. Tensile testing was carried out on an Instron Model 1125 displacement controlled machine at a displacement rate 0.02"/min. Load and strain gage were recorded using Macintosh based Lab View software.

The Integrated-Grip Specimen Configuration

The integrated-grip specimen was fabricated from the OS-4 composite panel with dimensions given in Figure 9. The interlacing surface pile in the OS-4 preform was woven over polycarbonate spacers. The preform was impregnated by the investigators in 3" x 5" x 2" sections utilizing a especially designed RTM mold. Preform compaction was not utilized in an effort to maintain the orthogonal orientation of the external surface piles. Therefore the fiber volume fraction of the OS-4 composite was similar to that of the preform (i.e., 45%). Following impregnation, void volume calculations according to ASTM D-3171 were performed on several specimens taken from the OS-4 test section. The measurements showed the OS-4 composite to have less than 2% voids which was deemed acceptable. The test section in OS-4 preform had an architecture identical to that of OS-3 preform. However, the actual post-processed architecture and fiber volume fractions of OS-4 composite were somewhat different than those of OS-3 composite due to the lack of compaction when processing the OS-4 composite panel.

The integrated-grip specimens were designed to utilize the same test section dimensions as those used with the bi-material specimen. However, stress singularity reduction by means of test section/transition section property matching or transition section notching were not exercised in the current specimen configuration due to material limitation. Such modifications can be implemented in the specimen design and will undoubtedly improve the results.

The integrated-grip specimens were prepared and tested along the orientations and under the conditions similar to the bi-material specimens.

Results and Discussion

Figure 10 shows a typical stress versus strain plot for a generation 3 bi-material specimen of TS-3 composite. Over 20 specimens were tested for each architecture and the elastic modulus and Poisson's ratio were determined from the initial straight region of each curve. Table 8 summarizes the average elastic properties obtained for the LS-3, TS-3 and OS-3 composites. The Table also lists values of the elastic modulus normalized to 60% fiber volume fraction to facilitate direct comparison of the composites.

Approximately 15 integrated-grip specimens of each orientation were tested and evaluated following the test methods described above. A typical stress versus strain curve for an OS-4 specimen is shown in Figure 11. A summary of the average elastic properties of the OS-4 composite are also presented in Table 8. Again, the measured elastic modulus has been normalized to 60 % fiber volume fraction to facilitate comparison with the properties of the LS-3, TS-3 and OS-3 composite panels.

As Figure 10 indicates, the bi-material specimen reached a maximum stress of only ~1900 psi (13 MPa) due to the failure of the adhesive bond. This failure level was seen to be very repeatable for the generation 3 specimen configuration. In comparison, interface failure levels for generation 2 specimen were typically 1500 psi (10.3 MPa), while generation 1 specimens showed typical interfacial failure stresses of 1200 psi (8.3 MPa). Examination of the generation 3 failure surface consistently showed that failure had occurred at or near the interface, showing evidence of carbon fiber tows having pulled out of the test section. The steady increase in interfacial failure stress from generation 1 to generation 3 specimen configuration shows the success of the singularity reduction scheme.

Direct comparison in Figure 12 of the measured elastic modulus, E33, for the three specimen generations of TS-3 composite shows that while the mean modulus is comparable within 12.8 %, there is a steady decrease in the variation of measured properties from generation 1 to generation 3 configuration. The error bars show one standard deviation range on either side of the mean. The reduction of the scatter in data again shows the effectiveness of interface singularity reduction. Of course some scatter is expected to exist due to experimental variations such as specimen location, local architecture, etc.

Comparing Figures 10 and 11 shows that the integrated-grip specimens failed at approximately 320% higher stress than the TS-3 bi-material specimens. Nevertheless, the OS-4 specimens still failed at the transition section/test section interface or in the grip section, thus preventing a strength measurement. Grip section failures were typically caused by preform imperfections. These imperfections were a result of surface pile tows in the preform interlacing several spacers. This caused the skewing of the spacers and the loss of orthogonality in the transition fiber tows which led to the premature failure within the transition section. In addition to preform imperfections in the transition section, numerous imperfections were observed in the fiber architecture of the OS-4 preforms within the test section. These imperfections are responsible for the large elastic modulus variation noted in the measured properties of the OS-4 composite.

Recommendations for Improvement of the Specimen Design

The failure stress in the bi-material specimen may be increased by using a lap joint configuration at the interface. The lap-joint would offer increased bonding surface over the current configuration and should help prevent premature first-layer fiber pull-out. A schematic of the proposed specimen configuration is presented in Figure 13. Preliminary analyses by the finite element method (FEM) have been performed to study the effects of the lap configuration on the stress field. The predicted through-the-thickness tensile stress profile is presented in Figure 14. The figure shows that the stress field is uniform in the major part of the test section.

The OS-4 preform was the first attempt by TTI at the design. Refining the preforming process in order to eliminate the processing imperfections would improve the failure strength and yield more reproducible data. Improvements in specimen design are also possible. The integrated-grip specimens used in the current investigation did not utilize material property matching between the transition and test sections. In the transition section there was no reinforcement along the warp direction and only polycarbonate spacers existed as "reinforcement" in the weft direction. The drastic in-plane property differences between the test and transition sections obviously resulted in a large stress singularity at the interface corners of the OS-4 specimens. This singularity could be reduced by replacing the polycarbonate spacers with graphite/epoxy laminate spacers of similar elastic properties and fiber volume fraction as the warp reinforcement of the test section.

In addition to including laminates as spacers, the use of stronger pile tows in the transition section than those utilized as through-the-thickness reinforcement in the test section could promote failure in the test section. Additionally, a dog-bone configuration could be utilized as presented in Figure 15. However, further stress analysis is required to determine optimum specimen configuration.

THROUGH-THE-THICKNESS COMPRESSION TESTING

Current Status of Compression Testing of Composite Materials

Compression testing of composite materials with laminated, 2D and 3D architectures has been an area of much research, as well as ambiguity. In general, compression test methods can be split into three categories based on the method of load introduction. The first type, designated indirect or shear loading, introduces a compressive stress field by shear loading the specimen through a fixture. Indirect methods include the IITRI, Celanese, and Lockheed test procedures. The second type, designated direct loading, applies the compressive load directly to the ends of the specimen such as in the NASA, NBS, Rockwell, Wright Patterson, RAE and ASTM-D695 procedures. The direct and indirect methods use both tabbed and untabbed specimens and specimens with lateral support of the gage section. The third specimen type is termed mixed loading and includes flexural test methods of honeycomb sandwich structures. [11]

Several studies comparing compression test methods for advanced composite materials have shown that while measured elastic properties are unaffected by the test method, the strength is strongly dependent on the specimen configuration and method of load application [11,12].

The main goals in the design of a compression specimen are to avoid Euler buckling and to yield a uniform stress field throughout as much of the specimen gage length as possible. Treating the specimen gage length as a homogeneous, orthotropic, simply-supported beam and without the consideration of shear deformations, the critical Euler buckling load [13] is given by

$$P_b = \frac{\pi^2 (w E_{ii} t^3)}{12 l^2 (1 - \upsilon_{ij} \upsilon_{ji})} \qquad \text{with } t < w \qquad (8)$$

where l, w, and t are the length, width, and thickness, respectively, of the specimen within the gage section; E_{ii} is the Young's modulus along the load direction; and ν_{ij} and ν_{ji} are the Poisson's ratios. The i and j subscripts denote directions parallel to the loading axis and perpendicular to the loading axis (i.e., parallel to the thickness direction of the specimen), respectively. When transverse shear deformation of the orthotropic material is included, the critical buckling load has been shown to be given by [14]

$$P_{cr} = \frac{P_b}{1 + 1.2 \cdot \frac{P_b}{A G_{ij}^{eff}}} \qquad (9)$$

Equation (9) represents a check on the measured strength. If the measured strength is close to the Euler buckling load, the specimen design is invalid and the gage length should be shortened. As Equation (9) shows, the critical load is a function of the material properties. Therefore, the required gage length can change with material system.

Specimen gage length also affects the uniformity of the stress field within the specimen test section. An analysis by Horgan [15] gives the following upper bound for Saint Venant's decay length, i.e., the distance from the load application point at which a uniform stress field is obtained

$$\lambda_{sv} = \frac{4.6}{2\pi} t \left(\frac{E_{ii}}{G_{ij}} \right)^{0.5} \qquad \text{for} \quad \frac{E_{ii}}{G_{ij}} >> 1 \qquad (10)$$

A detailed finite element analysis of the IITRI fixture by Bogetti et al. [14] showed the decay length for the specimen to be about 34% of that predicted by Equation (10). Thus the FEM-predicted decay length is approximately

$$\lambda_{fem} = \frac{t}{4} \left(\frac{E_{ii}}{G_{ij}} \right)^{0.5} \qquad (11)$$

From Equation (11), the minimum specimen gage length which will result in a uniform stress field at the midplane of the specimen is $2\,\lambda_{fem}$. This gives the following criterion for minimum gage length based on the stress field uniformity requirement

$$\frac{l}{t} > \frac{1}{2} \left(\frac{E_{ii}}{G_{ij}} \right)^{0.5} \qquad (12)$$

Therefore, Equations (9) and (12) provide the necessary specimen design constraints for valid compression testing.

Three main compressive failure modes have been observed for laminated composites [10,16,17]. These modes are: longitudinal matrix splitting, kink band formation and fiber microbuckling. Fiber microbuckling can occur in shear (in-phase buckling) or extensional modes (out-of-phase buckling). Fiber microbuckling is prominent in composite systems with low-modulus matrix materials. Several analytical models attempt to predict the critical microbuckling load for single fibers embedded in an infinite matrix and for fibers in a composite. Microbuckling loads are obtained by modeling the fibers as two-dimensional columns supported by an elastic foundation. Analyses show that the extensional mode dominates at low fiber volume fractions while the shear mode prevails at fiber volume fractions greater than 30%.

Following the methodology described above, Rosen [18] determined the critical microbuckling stress for the extensional mode to be

$$\sigma_{ce} = 2v_f \left[\frac{E_f E_m v_f}{3(1-v_f)} \right]^{0.5} \qquad (13)$$

where v_f is the fiber volume fraction along the load direction, E_f is the Young's modulus of the reinforcing fiber, and E_m is the Young's modulus of the matrix material. Similarly, the critical microbuckling stress for the shear mode was shown to be:

$$\sigma_{cs} = \frac{G_m}{(1-v_f)} \qquad (14)$$

where G_m is the matrix shear modulus and v_f is the fiber volume fraction along the load direction. Extensions of Rosen's work have been performed to include inelastic microbuckling and initial fiber misorientation [19, 20] .

As the modulus of the matrix material increases the compressive failure mode changes to kink band formation. Typically, kink bands originate at the specimen surface and propagate into the specimen. Kink band formation is random and total failure depends on the merging of the kinked regions. Analyses have shown that fiber kinking strongly depends on the extent of the initial fiber misorientation with respect to the load axis and the matrix yield strength. A detailed thermodynamic analysis by Evans and Adler [21] considers elastic strain energy in the fiber and matrix, plastic work in the matrix, and fiber fracture surface energy to predict kink angles and a failure criterion. A simplification of their analysis presented by Argon [22] shows the critical failure stress in compression to be

$$\sigma_c \approx \frac{\tau_{mys}}{\phi} \qquad (15)$$

where τ_{mys} is the matrix yield shear stress and ϕ is the initial misorientation in radians. The failure criterion offered by Evans and Adler includes statistical flaw distributions and probabilistic fiber fracture parameters.

A limited amount of experimental characterization of the compressive properties of 3D woven composite materials has been performed in the past [23-26]. Cox et al. [25] investigated the in-plane compressive behavior of layer-to-layer and through-the-thickness angle interlock woven carbon/epoxy composites. The failure mode was determined to be kinking of the warp stuffer tows. The final failure of the specimens was seen to be along a shear band. Total failure was assumed to occur at the formation of the second kink band. The critical load was determined from Equation (15) and measured misorintation angles. Good agreement was noted between the predicted critical loads and measured failure loads.

Design and Fabrication of 3D Woven Composite Specimens for Through-the-Thickness Compression Testing

The IITRI specimen configuration was selected for through-the-thickness compression testing of 3D woven composites in this investigation. Compression tests utilized the 1" thick LS-3, TS-3, and OS-3 composites. A bi-material compression specimen was designed following the methodology described above for through-the-thickness tensile testing. The bi-material compression specimen utilized 2D glass fabric reinforced epoxy composite transition sections for the grip area, along with standard glass/epoxy tabs to introduce a uniform compressive stress state into the 1" thick textile composite test coupon. A schematic of the specimen configuration used in the investigation is presented in Figure 16. The specimen thickness and width of 0.25" (6.35 mm) and 0.5" (12.7 mm), respectively, were selected based on the analysis of reference 6. The specimens utilized transition section material matching to minimize the stress singularity which exists at the corners of the test section/transition section interface [7]. Singularity reduction was implemented to ensure that failure occurred in the test section of the specimen and not in the adhesive layer. In order to select a gage length, the critical buckling load (Equation 9) and the critical stress decay length (Equation 11) were calculated using predicted elastic properties. The results are shown in Table 9. Critical lengths and buckling stresses were calculated for both the xz and yz orientations which were used to obtain v_{23} and v_{13}, respectively. These two orientations

required the use of predicted values of G_{23} and G_{13} in Equations (9) and (11). As Table 9 shows, the critical length for stress field uniformity is quite small. The small λ_{cr} is a result of the low degree of anisotropy which exists in the through-the-thickness direction. Since only about 10% of the total fiber volume is oriented in the thickness direction, E_{33} is low and λ_{cr} approaches values for isotropic materials. Since the stress decay length is less than 0.5", which is the recommended gage length for the ITTRI test, a gage length of 0.5" was selected for the specimens to ensure a uniform compressive stress field throughout the specimen gage length.

The test and transition sections were bonded together using American Cyanamid FM-300 film adhesive and a bonding fixture designed and fabricated by the authors. The bonding fixture ensured proper alignment and adequate bonding pressure. The specimens were cured at 350 °F for two hours. Following the adhesive cure, 0/90° strain gages were bonded to the test section of the specimen for strain measurement.

Compression Test Procedure

The bi-material specimens were tested in a displacement-control Instron Model 1125 testing machine at a displacement rate of 0.02 in/min (0.51 mm/min). Load and strain were monitored and stored by Macintosh-based Lab View software. Each specimen was tested until failure. Peak loads were noted and used to calculate the ultimate compressive stress, σ_c^{ult}, for each specimen.

Following the determination of an average σ_c^{ult} for each architecture, a second series of specimens was tested to various load levels to determine the failure mechanisms. Several specimens were loaded to levels near σ_c^{ult}. In the remaining specimens, the maximum load was reduced by steps of 1,000 lb (4.45 kN) to a minimum of 30% of the ultimate strength.

After testing, the surface of each specimen was examined by low-magnification optical microscopy to catalog the surface damage. Following surface inspection, the specimen was cut into four sections along the width direction and the sections were mounted and polished for optical microscopy. Damage modes such as matrix cracks, kink bands and transverse tow cracks were identified and cataloged.

Compression Test Results and Discussion

Elastic Compressive Properties

Elastic properties were obtained from at least five specimens for each architecture and both specimen orientations. Elastic modulus and Poisson's ratios were calculated from the stress-strain curves within the initial 2000 microstrain range. A typical stress-strain curve for an OS-3 specimen is presented in Figure 17. Each specimen tested showed linear behavior up to the maximum strain recorded by the strain gage. The average measured elastic properties for the LS-3, TS-3 and OS-3 composites are presented in Table 10. Measured elastic properties agreed well with the predicted properties presented in Table 5. Comparing the predicted and measured through-the-thickness compressive modulus, E_{33}^c, we find differences of -2.5%, -7.9% and -0.7% for the LS-3, TS-3 and OS-3 composites, respectively. The measured compressive elastic properties compare

favorably with the predicted properties and the measured through-the-thickness tensile elastic properties. The measured Poisson's ratios do not show as favorable an agreement with predictions as the Young's modulus. There are two possible reasons for this. First, the strain gages used to measure the Poisson's properties are much smaller than the dimensions of the macro-cell and are therefore not averaging the mechanical response of the material over an area comparable to that used in the model. Second, the low Poisson's ratios of these materials make accurate measurement of transverse strains extremely difficult.

Compressive Strength and Damage Progression

The peak load was used to calculate σ_c^{ult} for each specimen. The average values of σ_c^{ult} are presented in Table 11. The initial drop after the peak load coincided with splitting of surface warp or weft tows which were oriented perpendicular to the applied load. Beyond the peak load catastrophic failure of the specimen occurred, usually originating at split or damaged surface tows. The final failure appeared to follow the shear band mechanism discussed in the literature for in-plane compression of 3D woven composites [20-22]. However, the failure initiation by transverse surface tow splitting, and not kink band formation in the load bearing tows, made the through-the-thickness compressive failure mechanisms different from the in-plane mechanisms. The measured through-the-thickness strengths show little difference among the architectures. Also, for all architectures the xz specimen orientation produced lower measured strength than the yz orientation. These observations may imply that the failure of the composite is not controlled by the through-the-thickness warp weaver tows, but by the transverse (with respect to the load direction) warp stuffer and weft tows. The xz specimen orientation has the weft tows oriented out of the large 0.5 " (12.7 mm) x 0.5 " (12.7 mm) face (see Figure 16). This orientation has seven unsupported weft tows susceptible to transverse cracking, while the yz orientation has only six unsupported warp stuffer tows.

Microscopic inspections of the failed and damaged specimens indicated that surface tow splitting was the dominant failure mechanism for all three architectures. A summary of the damage progression observations is presented in Tables 12-14 and denotes similarity among the three architectures. Figure 18 documents the damage progression in the surface tows of LS-3 specimens loaded to 110 MPa, 165 MPa, 220 MPa and peak load, respectively. The figures show that damage increases with increased loading, and the orientation of the cracks implies shear damage (approximately ±45° to the loading direction).

As Tables 12-14 show, kink bands in the warp weaver (through-the-thickness) tows were present before the peak load was reached and therefore were not the direct cause of failure. As expected, the number of kink bands observed increased with increasing load. Kink bands are predicted to occur initially at regions of maximum misorientation with the applied load. This supposition was followed in some cases, but the writers observed that existing defects or damage seemed to be more responsible for the initial location and load at which kink bands formed. Several examples of observed kink bands near defects are presented in Figure 19.

In an attempt to ascertain that the observed kink bands were not the dominant failure mode, the critical load values predicted by the kink band model were calculated and compared to the measured values. The load on the warp weaver tows was determined by approximating the warp weaver stacks and the transverse tows as discrete layers. The modulus of the transverse tow layers was approximated by the lower bound rule of mixtures assuming a tow packing fraction of 80%. The warp weaver tow properties were obtained by transforming the axial tow properties with respect to the load axis. The angle of transformation is fixed by the weave architecture. The final load on the warp weaver layers was then calculated by assuming that an iso-stress condition existed in the through-the-thickness direction. Thus

$$\sigma_{33}^{ww} = \frac{\tau_{mys}}{\phi} \qquad (16)$$

at kink-band formation. Using Equation (16) , a matrix yield shear stress of 75 MPa ,and the warp weaver tow orientation, the critical kinking stress for each architecture was calculated and the results are summarized in Table 15. The misorientation angle ϕ was calculated with respect to the z axis and included an average tow distortion component. The tow distortion component was calculated from fiber volume fraction data and an assumed sinusoidal distortion path. As Table 15 shows the predicted kink-band stress corresponds nicely with kink-bands observed during the progressive damage study. The calculations also confirm that the kink-band failure mechanism is not the dominate failure mechanism for overall failure. Additional work is in progress to verify transverse tow failure mechanism as the true dominating failure mechanism.

THROUGH-THE-THICKNESS SHEAR TESTING

Specimen Design and Analysis

Numerous in-plane shear test methods have been developed to characterize the shear properties of composites with laminated and 2D preform architectures [27]. In reviewing these methods to determine the feasibility of modification for use in measuring through-the-thickness shear properties of 3D woven composites it was clear that many of them, including the torsional tube test method, the cross beam method, the Rail Shear method, the Arcan method, and the picture frame method, were unsuitable due to the complex methods of load introduction or the required specimen dimensions. Two test methods, namely the ASTM D-3846 Double Notch Shear (DNS) specimen and the Compact Shear (CS) specimen , appeared viable for utilization.

The Compact Shear specimen, shown in Figure 20, was recently developed by Ifju at Virginia Polytechnic Institute and successfully used to measure in-plane shear properties of cross-ply laminates and 3D woven composites [28]. The original specimen has dimensions of 1.5" x 1.5". However, because of the limited thickness of the composite panels (i.e., 1" for the thick panels in this investigation), the specimen dimensions have to be modified for application to through-the-thickness testing.

The standard ASTM D-3846 DNS specimen, also shown in Figure 20, has primarily been used to measure the interlaminar shear strength of laminated composites. Analysis of the specimen in [27] showed the shear stress field to be extremely nonuniform. Work by Bouette, Cazeneuve and Oytana [29] indicated that overlapping of the machined notches resulted in increased uniformity of the shear stress field in the gage section. Their work included a parametric FEM study to determine the effects of specimen gage length, L, and notch overlap, H, on shear stress field uniformity and tensile opening stresses. As with the CS specimen, the dimensions of the DNS specimen was modified for the measurement of through-the-thickness shear properties of 3D woven composites in this study. FEM analysis was conducted to examine stress distributions in the modified CS and DNS specimens. The results are presented below.

Modification and Analysis of the CS Specimen

Schematics of the two modified CS specimens used in this investigation are shown in Figure 21. The modified specimens are denoted TTIS1, which is used to measure the interlaminar shear properties, and TTIS2 which gives the transverse shear properties. Specimen performance

was judged by comparing the shear stress fields of Ifju's specimen, designated the baseline specimen, and the two modified specimens. Similarly, the transverse tensile stress fields were compared. The goal of the specimen modification was to create a specimen with shear stress field uniformity comparable to the baseline specimen and minimal transverse tensile stresses.

The FEM mesh used to analyze the baseline CS specimen is shown in Figure 22. Eight-node plain stress quadrilateral elements were used throughout the model. Boundary conditions were applied to approximate conditions existing in the fixture. It was assumed that the portion of the specimen clamped in the stationary half of the fixture had zero displacements in the x (or y depending on specimen orientation) and z directions. Similarly, the portion of the specimen clamped in the loaded half of the fixture was assumed to have zero displacements in the x (y) direction. Loading was approximated as a uniform pressure on the upper right arm of the specimen. Computations were performed for an applied pressure giving an average shear stress of 200 psi (1.38 MPa),where

$$P = \frac{\tau_{ij}^{ave} L}{A} \qquad (17)$$

where P is the applied pressure, τ_{ij}^{ave} is the average shear stress at the midplane of the specimen, and L and A are shown in Figure 21.

The FEM mesh was created using the commercial package PATRAN and solutions were obtained with ABAQUS. Normalized shear stress distributions along the gage length are presented in Figure 23 for the midplane (m=0) and planes at distances of m=0.05", m=0.10", and m=0.15" from the midplane. Figure 23 shows the shear stress field to be relatively uniform along the midplane. The magnitude of the stress in this plane is equal to τ_{ij}^{ave} over a z/L range of 0.3 to 0.6.

Figure 23 also presents the normalized transverse tensile stress field in the specimen gage section for the midplane and planes at distances of m=0.05", m=0.10", and m=0.15" from the midplane.. It is shown that the transverse tensile stress field is essentially zero in the majority of the specimen gage section. The results also show that the stress increases with increasing distance from the midplane and as the notches are approached.

Following the analysis of the baseline specimen, stress fields in the TTIS1 and the TTIS2 specimens were examined. The FEM meshes used for TTIS1 and TTIS2 specimens are also displayed in Figure 22. Eight-node plane stress quadrilateral elements and boundary conditions identical to those of the baseline specimen were adopted. The resulting shear and transverse tensile stress fields for a τ_{ij}^{ave} of 200 psi (1.38 MPa) are presented in Figures 24 and 25. The shear stress field for TTIS1 specimen (Figure 24) shows a loss in the symmetry of field compared to the baseline specimen. Conversely, the TTIS2 specimen maintains, if not improves, the field symmetry of the baseline specimen, but exhibits a plateau shear stress of approximately 1.05 times τ_{ij}^{ave} at the specimen midplane. Both specimen configurations displayed similar shear stress decrease with increasing distance from the midplane.

The shear stress fields in the modified TTIS1 and TTIS2 are altered only slightly from those in the baseline specimen. The significant area of the specimen is that covered by the strain gage. The dimensions of the shear gages utilized in this investigation are 0.75" (19 mm) x 0.125" (3.2 mm) for the TTIS1 specimen and 0.5"(12.7 mm) x 0.125" (6.35 mm) for the TTIS2

specimen. In an attempt to quantify the effects of the specimen modification, the average shear stress for planes at a constant distance from the midplane which would be covered by the strain gage was calculated, where

$$\tau_{ij}^{ave} = \frac{1}{L}\int_{L_o}^{L_f} \tau_{ij} dx_j \qquad (18)$$

where i = 3 and j=1,2 for the TTIS1 specimen, while i=1,2 and j=3 for the TTIS2 specimen; L_o and L_f denote the x_j coordinate of the notch tips for the upper notch and the lower notch, respectively. Equation (18) was approximated using nodal shear stress values according to the trapezoidal scheme, where

$$\tau_{ij}^{ave} = \frac{1}{L}\left[\frac{\tau_{ij}^{1}}{2}(x_j^2 - x_j^1) + \sum_{k=2}^{N-1}\tau_{ij}^{k}(x_j^k - x_j^{k-1}) + \frac{\tau_{ij}^{N}}{2}(x_j^N - x_j^{N-1})\right] \qquad (19)$$

where x_j's are the positions of the nodes along the specimen gage length, and N is the total number of nodes along a constant x_j plane. Average stresses were calculated for the specimen midplane and for positions at 0.05" and 0.10" from the midplane. The results of the estimated average stress state on each constant x plane for each specimen is presented in Table 16.

As Table 16 shows, the TTIS1 and TTIS2 specimen modifications only slightly affect the average stress in the specimen gage section. Comparing the two modified specimens with the baseline, the TTIS1 specimen shows a maximum difference with the baseline specimen of approximately 2.0% at the midplane and about 5.1% at 0.10" (2.54 mm) away from the midplane. The TTIS2 specimen shows slightly better agreement at the midplane with a difference of only 1.6% from the baseline specimen. The average shear stress along the midplane of the TTIS2 specimen is, however, closer to the desired average stress of 200 psi (1.378 MPa) than the baseline or TTIS1 specimens. The agreement with the baseline decreases slightly to a 10% difference at 0.10" away from the midplane. All three specimens show approximately a 15% drop in average shear stress at a distance of 0.10" away from the midplane. The analyses also show that for the measurement of strength, failure should occur at the specimen midplane, where

$$\tau_{ij}^{ult} = \frac{F}{LT} \qquad (20)$$

where F is the magnitude of the load applied to the arm of the specimen, L is the specimen gage length at the midplane, and T is the specimen thickness.

Modification and Analysis of the DNS Specimen

The goal of the parametric study was to maximize the degree of uniformity in the shear stress field in the specimen gage section while minimizing the tensile opening stress. The work of Bouette et al. and others has shown that the stress singularity at notch tips is reduced with increasing notch radius. Using this information a notch of radius of 0.03" (0.75mm) was used in the model. Several gage lengths ranging from 0.125" (3.2 mm) to 0.290" (7.4mm) were included in the study. Notch overlap ranges of 0 %, 10%, 20% and 50% of the specimen height of 0.25" (6.35 mm) were investigated.

A typical FEM mesh used in the investigation is shown in Figure 26. Eight-node plane stress quadrilateral elements were used throughout the entire model. The ASTM D-3846 method utilizes a steel clamp, shown in Figure 20, to prevent specimen buckling. However, the small size of the suggested specimen precludes the use of such a clamp here. The specimen is loaded directly in compression between two platens. This loading condition was modeled as zero displacements along the lower platen and as a uniform pressure field at the upper platen.

Following the methodology of the CS specimen analysis, pressure was applied to produce an average shear stress of 200 psi (1.378 MPa) at the midplane of the specimen. The magnitude of the applied pressure is again determined using equation (17) with the dimension A being replaced by the notch spacing L. Models were run for L values of 0.125" (3.2 mm), 0.250" (6.35 mm) and 0.29" (7.4 mm) and H (notch overlap) values of 0%, 10%, 20% and 50% of the specimen thickness for each L condition.

The results, shown in Figure 27, for a gage length of 0.290" are similar to those obtained by Bouette et al. It is seen that increasing the notch overlap improves the symmetry of the stress distribution on each constant x plane, and brings the average shear stress on the midplane closer to the desired τ_{ij}^{ave} of 200 psi. Also, the shear stress profile symmetry decreases with increasing gage length. These trends are quantified in Table 17 which presents the average shear stresses from equation (19) for the specimen midplane and at 0.025" and 0.05" away from the midplane. Table 17 showes that the notch overlap, H, controls the uniformity of the shear stress distribution in the x (y) direction. The distribution is important in elastic property measurement. If the change in average stress between x (y) planes is small, standard strain gages can be effectively used to measure through-the-thickness shear muduli.

In addition to shear stress field uniformity, minimization of tensile opening stresses was desirable to ensure failure in shear. Figure 28 shows the effect of increasing L on the transverse tensile stress distribution at the specimen midplane for H =0%. Increasing L and H increased the maximum tensile stress observed near the notch. raising the H was shown to raise the predicted maximum tensile stress. The maximum opening tensile stress predicted was approximately 4 times the average shear stress, which was seen for the specimen with L=0.290" (7.4 mm) and H=50%.

The FEM analysis revealed the need for the design of two distinct specimen configurations; one for the measurement of the elastic shear properties and the other for the determination of shear strength. In an attempt to capture as much of the through-the-thickness repeat structure as possible for elastic property measurement, the final dimensions of the elastic property specimen were selected as L=0.290" (7.4 mm) and H=50%. The strength specimen required minimizing L to reduce transverse tensile stresses. However, as with the elastic property measurement, testing of the entire repeat structure was desirable. Therefore, it was decided that several specimens with different gage lengths would be used, all with H=20%. The H value of 20% was used to ensure that the average shear stress in the specimen midplane was in fact the desired stress as calculated by equation (20). Schematics of the final specimen dimensions are presented in Figure 29.

Shear Specimen Fabrication and Testing Procedures

Both the TTIS1 and TTIS2 specimen configurations were utilized in testing for through-the-thickness properties of the LS-3 composite panel. Due to lack of material, only the TTIS1 specimen configuration was used with the TS-3 and OS-3 panels. Each specimen was prepared and tested in two orientations to measure the various through-the-thickness shear properties. Table

18 lists the specimen orientations and the properties determined for each specimen and orientation . The orientation was defined by the plane on which the shear stress was applied (See Figure 21). The TTIS2 specimen configuration gives the transverse shear properties while the TTIS1 configuration yields the interlaminar shear properties.

Specimens were cut from the composite panels using a water-lubricated, diamond-coated cut-off wheel. Following the cutting procedure, notches were machined into each coupon using a 0.25" (6.35 mm) diameter endmill. Next, strain gages were bonded to the surface of each specimen as shown in Figure 21. Both TTIS1 and TTIS2 specimens were tested in the fixture developed by Ifju. The fixture was designed to accommodate 1.5" (38 mm) x 1.5" (38 mm) specimens. Since the TTIS2 specimen is only 1" (25.4mm) long in the load direction composite spacers were fabricated and used to support the specimen in the fixture.

Due to lack of material, the modified DNS specimen was used only for the OS-3 composite to determine G_{13} and τ_{13} properties. coupons, 0.50"x 0.50"x1.0", were cut from the OS-3 panel in the yz orientation. Notches were machined into each specimen using a slot grinding machine fitted with a diamond-coated wheel. Following the notching procedure, 0.0625" (1.6 mm) shear strain gages were bonded onto the specimen at the center of the gage length as shown in Figure 29. The strain gages covered approximately 80% of the specimen gage section.

In addition to the 1" thick composites, interlaminar shear strength tests were also performed on the 0.25" thick LS-1, LS-2, TS-1 and TS-2 panels. Shear strengths were measured using standard ASTM D3846-79 specimens shown in Figure 20. Two specimen orientations were tested to obtain shear strengths τ_{31} and τ_{32}. The τ_{31} was obtained by imparting a compressive load along the warp tows, while the τ_{32} was measured by applying a compressive load along the weft tows.

All shear tests were conducted in an Instron 1125 displacement-controlled machine at a displacement rate of 0.02"/min (0.71 mm/min). Load and strain were monitored and stored using Macintosh supported Lab View software.

Shear Test Results and Discussion

Elastic Shear Properties

Summaries of measured elastic shear moduli for each composite architecture and specimen configuration are presented in Table 19. Representative stress vs. strain plots obtained from the TTIS1 and TTIS2 specimen configurations are shown in Figures 30 and 31, respectively. The materials tested typically showed large regions of linear response followed by non-linear response.

Comparing measured elastic moduli for the LS-3 composite in Table 19, it is noted that for identical shear couples the moduli are nearly equivalent. A statistical analysis, using t-test with a confidence level of 95%, was performed on the raw data to check for the equivalency of measured G_{13} and G_{23} (TTIS2 configuration) with G_{31} and G_{32} (TTIS1 configuration). The following null and alternative hypothesis were proposed:

$$H_0: G_{13}^{TTIS2} = G_{31}^{TTIS1}$$
$$H_1: G_{13}^{TTIS2} \neq G_{31}^{TTIS1} \qquad (21)$$

and

$$H_0: G_{23}^{TTIS2} = G_{32}^{TTIS1}$$
$$H_1: G_{23}^{TTIS2} \neq G_{32}^{TTIS1} \quad (22)$$

The values of t were calculated using equation (16) shown below.

$$t = \frac{\overline{X_1} - \overline{X_2}}{\sqrt{\frac{s_1^2}{n_1} + \frac{s_2^2}{n_2}}} \quad (23)$$

where $\overline{X_1}$ and $\overline{X_2}$ are the means of the measured properties, s_1, and s_2 are the standard deviations of the measured properties and n_1 and n_2 are the number of samples in each population. The critical t value obtained from standard statistical tables is 1.79. [30] Inserting the statistical data for the LS-3 composite for each orientation, the calculated t values were 0.40 and 0.29 for the G_{13}/G_{31} and G_{23}/G_{32} pairs, respectively. Since both these values are less than the critical t value the proposed hypotheses in equations (21) and (22) are accepted showing equivalent measured properties for the TTIS1 and TTIS2 specimen configurations.

A similar statistical analysis was performed on the measured G_{13}/G_{31} properties for the OS-3 composite. The G_{13} data were obtained with the modified DNS specimen while the G_{31} data were determined from the TTIS1 specimen. A t-test on the difference in measured means was again performed against the following null and alternative hypothesis

$$H_o: G_{13}^{DNSS} = G_{13}^{CSS}$$
$$H_1: G_{13}^{DNSS} \neq G_{13}^{CSS} \quad (24)$$

A 95% confidence level was utilized leading to a critical t value of 1.79. The value of t from equation (23) is 0.404 which again is less than the critical level indicating that the measured G_{13} and G_{31} are statistically equivalent.

From a testing standpoint, the modified CS specimens were easier to fabricate and to use. The modified CS specimen fabrication procedure involved only cutting 1.0" (25.4 mm) x 1.5" (38 mm) coupons and milling the notches. Conversely, the modified DNS specimens involved the use of a milling machine to notch the sample which resulted in less accurate specimen dimensions and increased fabrication times. Additionally, less of the stress-strain curve of the material was obtained with the modified DNS due to specimen bending which resulted in touching of the opposite notch surfaces. The specimen bending was due to the large notch overlap required in the DNS specimen for a uniform shear stress field. Also, the composite through-the-thickness stiffness is extremely low which allows bending of the DNS specimen ligaments and subsequent notch closure. For elastic property measurement the modified CS specimen showed superior performance and ease of fabrication and is therefore recommended over the modified DNS specimen.

Shear Strengths

Strength data were successfully obtained from the TTIS1 specimen (interlaminar shear strength) but not the TTIS2 or the modified DNSS specimen configurations (transverse shear strength). The TTIS2 specimens failed prematurely in the specimen arm. The modified DNS

specimens also failed prematurely in bending in the ligament directly under the notch. As described earlier, notch overlaps of H=20% were utilized to ensure uniform shear stress fields. This specimen configuration allowed ligament bending and subsequent touching of the notch faces. Specimens with no notch overlap (H=0%) were fabricated, despite the non-uniform stress distribution, and tested in attempts to obtain some indication of the through-the-thickness shear strength. However, strength values were still not obtained due to notch closure. The inability of the DNS specimen to yield strength was due to the low through-the-thickness stiffness of the composite panels. The through-the-thickness stiffness of each panel is under 2 Msi (13.8 GPa) which allows the opposite faces of the notches to touch prior to failure in the gage section of the specimen. The notch closure problem could possibly be eliminated with the fabrication of a compatible restraining jig similar to the one used in the standard DNS specimen.

The failures observed in the TTIS1 specimen configuration followed tow interfaces in the specimen gage section . In fact, if tows fell along the midplane of the specimen failure would still occur at the tow interfaces away from the specimen midplane. The interlaminar shear strengths (τ_{31} and τ_{32}) obtained from the TTIS1 specimen configuration are summarized in Table 20.

The failure of the modified specimens to measure transverse shear strength components was due in part to the fiber/matrix interfacial properties. Failure in through-the-thickness shear required failure of fibers in the warp and weft tows while the interlaminar failure merely involved interfacial failure between the matrix and tows.

A summary of the interlaminar shear strengths of the 0.25" composite panels is presented in Table 21. For all of the four architectures tested the shear strength τ_{31} is greater than τ_{32}. Also, the TS architecture provides a higher interlaminar shear strength than the LS architecture. These trends follow the expectation. The τ_{31} shear strength is larger because the loading direction is parallel to the warp weaver tows. Similarly, the TS architectures provide superior strength since the entire thickness of the plate is interlaced by the warp weaver tows, not just the adjacent layers as in the LS architecture.

Shear failure mechanisms were similar in all architectures. Failure initiated at the notch tips and propagated throughout the remainder of the test region along the interface of warp and weft tow stacks. Typical failures showed the through-the-thickness reinforcement to remain intact and bridge the failed interface regions. The bridging, however, did not provide any load transfer. Thus, despite the through-the-thickness reinforcement, the interlaminar strength was still a matrix dominated property.

Comparison of the interlaminar shear strengths measured from the 0.25" panels and the 1" panels shows comparable performance between the 1" and 0.25" panels. Table 22 presents the measured interlaminar shear strengths for all the architectures normalized to 60 % overall fiber volume fraction.

CONCLUSIONS

Characterization of the composites microstructures revealed significant distortion of the architecture due to compaction during the RTM processing. Distortion of the through-the-thickness tows was particularly severe in the OS-3 composite and is believed to be the primary reason for the lower through-the-thickness Young's modulus of this composite compared to LS-3 and TS-3 panels. The volume averaging model used in this investigation for the prediction of the composite elastic moduli was modified to include the effect of the processing-induced tow

undulations. Without such modification the model significantly over-predicted the elastic properties.

A bi-material specimen, consisting of a test section and transition sections, was designed and evaluated for the direct measurement of through-the-thickness tensile behavior of 3D textile composites. This specimen utilized 1" thick composite panels (i.e., LS-3, TS-3, and OS-3). Design optimizations obtained from a Boundary Element Analysis were implemented and proven successful. The adhesively-bonded bi-material specimen with optimized configuration was effective in providing the through-the-thickness elastic moduli but its early failure at the bonded joint rendered it unsuitable for strength measurement. The experimentally determined Young's modulus, E_{33}, and Poisson's ratios, ν_{13} and ν_{23}, agreed reasonably well with predicted values. An orthogonal woven preform with surface pile was designed which allowed the fabrication of a bi-material specimen with integrally woven transition sections. This specimen resulted in over 300% improvement in the failure stress over the bonded specimen, however, premature failure still occurred near the grip region due to architectural imperfections in the preform and no attempt to optimize the transition section properties or the specimen geometry. Recommendations for improvements of the bonded and integrated-grip tensile specimens have been proposed.

The bi-material specimen was also used for through-the-thickness compression testing using the ITTRI compression fixture. Both, through-the-thickness compressive strength and elastic moduli were measured. The compressive elastic modulus and Poisson's ratios agreed well with those obtained from tensile tests as well as the predicted values. Investigation of the compressive failure mechanisms showed that although kink bands occurred, they were not responsible for the composite final failure. Final failure was due to transverse tow splitting.

Two modified Compact Shear and a modified Double Notch Shear specimens were used for the determination of both transverse and interlaminar shear strengths and elastic moduli. These specimens utilized 1" thick composite panels. Both specimen configurations proved successful for the determination of the through-the-thickness shear elastic moduli. The experimental values of shear moduli agreed well with theoretical predictions. While both specimen configurations will provide accurate elastic properties, the modified CS configurations are recommended due to the ease of fabrication and the ability of the specimen to measure a wider range of the stress-strain curve.

The interlaminar shear strength was successfully determined from the modified CS specimen (TTIS1). But neither the modified CS (TTIS2) nor the modified DNS specimens could provide a measurement of the transverse shear strength. The TTIS2 specimens failed in the specimen arm while the modified DNS specimens exhibited premature failure under the notches due to specimen bending. Strength properties could possibly be obtained using the modified DNS specimen with the use of a restraining jig, or by incorporating tabbing material onto the arms of the TTIS2 specimen.

Interlaminar shear strengths were also determined for the 0.25" woven panels (i.e., LS-1, LS-2, TS-1, and TS-2) using the modified DNS specimen. Comparable performance was observed between the 0.25" and the 1" composite panels. For all the composites tested, the τ_{31} strength was larger than the τ_{32} strength. Also, the through-the-thickness angle interlock architecture gave superior interlaminar shear strength than the layer-to-layer angle interlock architecture.

ACKNOWLEDGMENT

This work was supported by NASA Langley Research Center under contract Number NAG-1-1383. The authors would like to thank Dr. Peter Ifju of the University of Florida for supplying the fixture for compact shear testing.

REFERENCES

[1] Byun, J. H., Leach, B. S., Stroud, S. S. and Chou, T. W.: Structural Characteristics of Three-Dimensional Angle-Interlock Woven Fabric Preforms. in Processing of Polymers and Polymeric Composites, ASME, MD-, vol. 19, American Society for Mechanical Engineers, New York, 1989, p. 177.

[2] Chou, T. W. and Yang, J. M.: Structure-Performance Maps of Polymeric Metal and Ceramic Matrix Composites. *Metall. Trans. A,* vol. 17, 1986, pp. 1547-9.

[3] Ma, C. L., Yang, J. M. and Chou, T. W.: Elastic Stiffness of Three-Timensional Braided Textile Structural Composites. in Composite Materials, Testing and Design (Seventh Conference), ASTM STP 893, American Society for Testing and Materials, Philadelphia, PA, 1986, pp. 404-21.

[4] Yang, J. M., Ma, C. L. and Chou, T. W.: Fiber Inclination Model of Three-Dimensional Textile Structural Composites. *J. Comp. Mat.,* Vol. 20, No. 5, 1986, pp. 472-84.

[5] Majidi, A. P., Yang, J. M., Pipes, R. B. and Chou, T. W.: Mechanical Behavior of Three-Dimensional Woven Fiber Composites. in Proceedings of the Fifth International Conference on composite Materials, The Metallurgical Society of AIME, Warrendale, PA, 1986, pp. 1247-65.

[6] Pochiraju, K., Majidi, A. P. and Chou, T. W.: Theoretical and Experimental Characterization of 3-D Woven and Braided Textile Composites. ICCE-1, New Orleans, LA, 1994.

[7] Shan, H. Z., Majidi, A. P. and Chou, T. W.: Numerical Analysis for Design of Composite Specimens for Through-the-Thickness Tensile Measurements. *J. Comp. Mat.*, Vol. 28, 1994, pp. 1032-56.

[8] Byun, J. H.: Process-Microstructure-Performance Relationships of Three-Dimensional Textile Composites. Ph.D Thesis, University of Delaware, Newark, DE, 1991.

[9] Hull, D.: An Introduction to Composite Materials. Cambridge University Press. Cambridge, 1981, pp. 103-121.

[10] Steenkamer, D.: The Influence of Preform Design and Manufacturing Issues on the Processing and Performance of Resin Transfer Molded Composites. Ph. D. Thesis, University of Delaware, Newark, DE, 1993.

[11] Camponesch, E. T., and K. O'Brien: Compression of Composite Materials: a Review. *ASTM STP 1110* , American Society for Testing and Materials, Philadelphia, PA, 1991, pp. 550-578

[12] Haberle J. G., and Matthews F.L.: The Influence of Test Method on the Compressive Strength of Several Fiber-Reinforced Plastics. *J. of Advanced Mat.,* Oct. 1993, pp. 35-45.

[13] Timoshenko, S.P., Theory of Elastic Stability, 1st edition, McGraw-Hill, New York, New York, 1936.

[14] Bogetti, T. A., Geillespie, J. W. and Pipes, R. B.: Evaluation of the IITRI Compression Test Method for Stiffness and Strength Determination. *Composites Science and Technology* , Vol 32, No. 1, 1988, pp. 57-76.

[15] Horgan, C. O.: Some Remarks on Saint-Venant's Principle for Transversely Isotropic Composites, *Journal of Elasticity,* Vol. 2, 1972, pp. 335-9.

[16] Hahn, H. T., Williams, J. G., and J. M. Whitney, Ed.: Compression Failure Mechanisms in Unidirectional Composites. *Composite Materials: Testing and Design (Seventh Conference), ASTM STP 893.* American Society for Testing and Materials, Phiadelphia, PA, 1986, pp. 115-39.

[17] Greszczuk, L. B.: Compressive Strength and Failure Modes of Unidirectional Composites. *Analysis of the Test Methods for High Modulus Fibers and Composites ASTM STP 521*, American Society for Testing and Materials, Philadelphia, PA, 1973, pp. 192-217.

[18] Rosen, B. W.: in *Fiber Composite Materials*, American Society of Metals, Metals Park, Ohio, 1965, Chapter 3.

[19] Schurerch, H.: *American Institute of Aeronatucs and Astronautcs Journal.,* Vol. 4, No. 1, 1966, pp. 102-6.

[20] Slaughter, W. S. and Fleck, N. A.: Viscoelastic Microbuckling of Fiber Composites. *Journal of Applied Mechanics, Trans. of the ASME,* Vol. 60, No. 4, 1993, pp. 803-806.

[21] Evans, A.G. and Adler, W. F.: Kinking as a Mode of Structural Degradation in Carbon Fiber Composites. *Acta. Metallurgica* , Vol. 26, 1978, pp. 725-738.

[22] Argon, A. S.: Fracture of Composites. *Treeatise of Materials Science and Technology*, Vol 1., Academic Press, New York, 1972. pp 106-114.

[23] Guess, T. R. and Reedy E. D.: *J. Comp. Tech Res.*, Vol. 7, 1986, p. 136.

[24] Guess, T. R. and Reedy E. D.: *J. Comp. Tech Res.,* Vol. 8, 1986, p. 163.

[25] Cox, B.N., Dadkhah, M.S., Inman R. V., Morris, W. L. and Zupon, J.: Mechanisms of Compressive Failure in 3D Composites. *Acta metall .mater.,* Vol. 40, No. 12., 1992, pp. 3285-3298.

[26] Weaver, C.W. and Williams J., G.: Deformation of a Carbon-Epoxy Composite Under Hydrostatic Pressure. *Journal of Materials Science.,* Vol. 10, 1975, pp. 1323-1333.

[27] Chaterjee, S., Adams, D. and Oplinger D. W.: Test Methods for Composites a Status Report. DOT/FAA/CT Report-93/17, III. June 1993.

[28] Ifju, P. NASA Textile Mechanics Workgroup Progress Report. July 1993.

[29] Bouette, B.; Cazeneuve, C.; Oytan, C.: Effect of Strain Rate on Interlaminar Shear Properties of Carbon/Epoxy Composites. *Composite Sciece and Technology*, Vol. 45, No. 4, 1992, pp 313-324.

[30] Hogg, R. V. and Ledolter, J., *Engineering Statistics* , Macmillan Publinshing Company, New York, 1987, p. 397.

Table 1 - Descriptions of the Fiber Architectures

Desig.	Architecture	Nominal Thickness in (mm)	Tow Size K		
			Warp Stuffer	Warp Weaver	Weft
LS-1	Layer-to-layer angle interlock	0.25 (6.35)	24	6	12
LS-2	Layer-to-layer angle interlock	0.25 (6.35)	12	3	6
LS-3	Layer-to-layer angle interlock	1.00 (25.4)	60	6	24
TS-1	Through-the-thickness angle interlock	0.25 (6.35)	24	6	12
TS-2	Through-the-thickness angle interlock	0.25 (6.35)	12	3	6
TS-3	Through-the-thickness angle interlock	1.00 (25.4)	60	6	24
OS-2	Through-the-thickness orthogonal	0.25 (6.35)	12	3	6
OS-3	Through-the-thickness orthogonal	1.00 (25.4)	60	6	24
OS-4	Through-the-thickness orthogonal	1.00 (25.4)	60	6	24

Table 2 - Overal and Directional Fiber Volume Fractions

Architecture	Overall Fiber Vol. %	Warp Stuffer %	Weft %	Warp Weaver %
LS-1	57.80±0.78	32.5	20.4	4.9
LS-2	60.29±1.72	33.2	24.7	2.4
LS-3	58.95±0.68	27.8	18.6	12.6
TS-1	60.69±1.82	33.6	18.9	8.1
TS-2	58.05±0.40	29.4	21.8	7.0
TS-3	62.30±1.12	33.3	20.9	8.1
OS-3	63.10±2.36	30.4	16.6	16.1
OS-4	44.50±1.50	21.4	11.7	11.4

Table 3 - Unit Cell Dimensions

Composite	a (mm)	b (mm)	c (mm)
LS-1	4.26	9.00	1.39
LS-2	3.12	14.31	1.04
LS-3	4.20	2.13	2.81
TS-1	11.18	12.34	5.72
TS-2	12.34	1.78	5.72
TS-3	2.00	2.14	2.85
OS-3	2.42	2.24	2.90

Table 4 - Macro-Cell Dimensions

Composite	a (mm)	b (mm)	c (mm)
LS-1	9.52	9.00	5.72
LS-2	8.89	14.31	5.72
LS-3	8.41	2.13	25.40
TS-1	22.36	8.90	5.76
TS-2	24.68	10.68	5.75
TS-3	16.44	2.14	25.40
OS-3	4.84	2.24	25.40

Table 5 - Predicted Elastic Properties Using Volume Averaging Method

Composite	E_{11} (GPa)	E_{22} (GPa)	E_{33} (GPa)	G_{23} (GPa)	G_{13} (GPa)	G_{12} (GPa)	ν_{23}	ν_{13}	ν_{12}
LS-1	90.2	55.8	9.6	6.2	6.4	6.2	0.054	0.039	0.030
LS-2	87.3	65.4	10.1	6.5	6.7	6.5	0.048	0.041	0.028
LS-3	79.1	53.5	12.0	6.3	6.7	6.3	0.051	0.047	0.040
TS-1	86.1	53.3	13.4	6.6	6.9	6.6	0.053	0.038	0.035
TS-2	75.8	59.3	12.2	6.2	6.4	6.2	0.046	0.40	0.051
TS-3	84.9	59.1	12.5	6.8	7.0	6.8	0.050	0.051	0.036
OS-3	85.4	49.9	13.4	6.9	7.7	6.9	0.058	0.061	0.033

Table 6 - Glass Fabric/Epoxy Mechanical Property Data

Fabric Type	Test Direction	Weight Fraction	E_{11} (GPa)	ν_{12}
Continuous Strand Mat.	Warp	0.281	7.16	0.30
Continuous Strand Mat.	Warp	0.367	8.41	0.31
Continuous Strand Mat.	Warp	0.431	9.57	0.29
0/90/C	Warp	0.645	21.56	0.18
0/90/C	Warp	0.774	28.89	0.17
0/90	Warp	0.617	21.42	0.18
0/90	Warp	0.672	24.46	0.16
0/90	Warp	0.707	28.87	0.13
45/C	Warp	0.616	14.67	0.42
45/C	Warp	0.704	17.77	0.39

Table 7- Transition Section/Test Section Combinations for Bi-Material Specimen

Composite	Orientation	Transition Section Material	α
LS-3	XZ	0/90 (W_f=0.707)	0.011
LS-3	YZ	0/90 (W_f=0.707)	0.009
TS-3	XZ	0/90 (W_f=0.707)	0.011
TS-3	YZ	0/90 (W_f=0.707)	0.013
OS-3	XZ	0/90 (W_f=0.707)	0.015
OS-3	YZ	0/90 (W_f=0.707)	0.012

Table 8 - Summary of Measured Through-the-Thickness Tensile Properties

Architecture	E_{33} (GPa)	Normalized To 60% E_{33} (GPa)	ν_{13}	ν_{23}
LS-3	11.62±2.28	11.82	0.050±0.011	0.101±0.023
TS-3	12.18±2.28	11.73	0.083±0.012	0.186±0.015
OS-3	11.11±3.84	10.56	-	0.0698±0.021
OS-4	8.58±5.49	11.56	0.0341±0.0078	0.1040±0.032

Table 9 - Critical Stress Decay Length and Critical Buckling Stress

Specimen	E_{33} (GPa)	G_{13} (GPa)	G_{23} (GPa)	λ_{cr} (mm)	l (mm)	σ_{cr} (MPa)
LS3-XZ	12.0	6.75	6.34	4.37	12.7	1697
LS3-YZ	12.0	6.75	6.34	4.23	12.7	1731
TS3-XZ	12.6	7.23	6.86	4.30	12.7	1801
TS3-YZ	12.6	7.23	6.86	4.19	12.7	1831
OS3-XZ	13.4	7.65	7.03	4.33	12.7	1863
OS3-YZ	13.4	7.65	6.95	4.16	12.7	1912

Table 10 - Summary of Measured Compressive Elastic Properties

Composite	E_{33} (GPa)	ν_{13}	ν_{23}
LS-3	12.3 ± 2.8	0.038 ± 0.005	0.122 ± 0.041
TS-3	13.6 ± 1.8	0.059 ± 0.031	0.070 ± 0.030
OS-3	13.3 ± 3.2	0.043 ± 0.017	0.185 ± 0.074

Table 11 - Summary of Measured Ultimate compressive Strengths.

Composite	Orientation	σ_c^{ult} (MPa)
LS-3	XZ	374.9 ± 22.9
LS-3	YZ	412.5 ± 19.0
TS-3	XZ	345.8 ± 1.62
TS-3	YZ	402.5 ± 11.4
OS-3	XZ	361.6 ± 25.4
OS-3	YZ	411.2 ± 26.9

Table 12 - Damage Progression in LS-3 Composite

Applied Stress (MPa)	% of Average Failure Stress	Observed Damage
110	26.7	• Several matrix cracks originating at voids noted • Matrix cracks concentrated near bi-material interface
165	40.1	• Density of matrix cracks increased greatly • Kink bands noted in several warp weaver tows • Several cracks oriented at approximately ±45° noted in surface warp stuffer tows
220	53.5	• Matrix crack density and kink band density increased • Degree of cracking in surface warp stuffer tows increased.
Peak	100	• Matrix crack density and kink band density increased • Total splitting of surface warp stuffer tow observed

Table 13 - Damage Progression in TS-3 Composite

Applied Stress (MPa)	% of Average Failure Stress	Observed Damage
220	54.7	• Several matrix cracks originating at voids noted. • No kink bands observed in any of the viewed cross-sections. • Cracks starting to form in surface warp stuffer tows.
275	68.6	• Density of matrix cracks increased greatly. • Kink bands noted in several warp weaver tows. • Significant cracking seen in surface warp stuffer tows.
330	82.3	• Matrix crack density and kink band density increased • Degree of cracking in surface warp stuffer tows increased.
Peak	100	• Matrix crack density and kink band density increased • Total splitting of surface warp stuffer tow observed

Table 14 - Damage Progression in OS-3 Composite

Applied Stress (MPa)	% of Average Failure Stress	Observed Damage
165	40.1	• Matrix cracks noted • Preliminary kink bands noted
275	67.1	• Density of matrix cracks increased greatly • Kink bands noted in several warp weaver tows • Several cracks oriented at approximately $\pm 45^{o}$ noted in surface warp stuffer tows
330	80.0	• Numerous kink bands in through-the-thickness tows • Cracking in warp surface tows increased
Peak	100	• Matrix crack density and kink band density increased • Total splitting of surface warp stuffer tow observed

Table 15 - Critical Stresses Predicted from Kink Band Model

Composite	ϕ (radians)	σ_c (MPa)
LS-3	0.61	124.0
TS-3	0.574	130.7
OS-3	0.496	151.2

Table 16 - Average Stresses Along Planes at Different Positions for Baseline and Modified CS Specimens

Specimen	Midplane psi (MPa)	Midplane+0.05" psi (MPa)	MidPlane+0.10" psi (MPa)
Baseline	204.2 (1.407)	199.0 (1.371)	174.7 (1.203)
TTIS1	208.3 (1.435)	199.2 (1.372)	165.7 (1.142)
TTIS2	201.0 (1.385)	199.8 (1.377)	157.0 (1.082)

Table 17 - Average Stresses Along Planes at Different Positions for Modified DNS Specimen

Gage Length (L) (in/mm)	Notch Overlap (H) %	$\tau_{i\,3}^{ave}$ x=0.000 psi (MPa)	$\tau_{i\,3}^{ave}$ x=0.025" psi (MPa)	$\tau_{i\,3}^{ave}$ x=0.050" psi (MPa)
0.125 / 3.2	0	134.7	121.4	70.9
0.125 / 3.2	10	176.1	132.1	87.3
0.125 / 3.2	20	200.6	150.8	106.5
0.125 / 3.2	50	199.8	199.5	191.8
0.250 / 6.35	0	148.8	129.2	96.1
0.250 / 6.35	10	188.3	141.8	104.1
0.250 / 6.35	20	198.5	165.1	121.4
0.250 / 6.35	50	199.9	199.8	187.0
0.290 / 7.4	0	148.9	131.5	98.1
0.290 / 7.4	10	189.9	143.1	105.4
0.290 / 7.4	20	199.5	165.6	122.8
0.290 / 7.4	50	199.7	199.9	181.7

Table 18 - Test Matrix for Modified CS Specimens

Specimen	Orientation	Measured Elastic Property	Measured Strength Property
TTIS1	XY	G_{31}	τ_{31}
TTIS1	YX	G_{32}	τ_{32}
TTIS2	XZ	G_{23}	τ_{23}
TTIS2	YZ	G_{13}	τ_{13}

Table 19 - Summary of Measured Properties Using Modified CS Specimens

Composite	G_{13} Msi (GPa)	G_{31} Msi (GPa)	G_{23} Msi (GPa)	G_{32} Msi (GPa)
LS-3	1.01±0.26 (6.96±1.8)	1.07±0.30 (7.37±2.06)	0.836 ± 0.11 (5.76 ±0.75)	0.815 ± 0.14 (5.61± 0.98)
TS-3	-	0.761 ± 0.06 (5.24 ± 0.42)	-	0.900 ± 0.06 (6.2 ± 0.42)
OS-3	-	0.895±0.03 (6.17 ± 0.17)	-	0.846± 0.05 (5.83 ± 0.36)

Table 20 - Summary of τ_{31} and τ_{32} Strength Data Obtained with TTIS1 Specimen Configuration

Composite	τ_{31} psi (MPa)	τ_{32} psi (MPa)
LS-3	3820 ± 310 (26.3 ± 2.1)	3365 ± 273 (23.2 ± 1.9)
TS-3	4270 ± 750 (29.4 ± 5.2)	3830 ± 345 (26.4 ± 2.4)
OS-3	4980 ± 927 (34.3 ± 6.4)	5370 ± 693 (37.0 ± 4.8)

Table 21 - Interlaminar Shear Strength Data from 0.25" Panels

Architecture	Shear Strength Tested	Measured Shear Strength psi (MPa)
LS-1	τ_{31}	4230±695 (29.0±4.8)
LS-1	τ_{32}	3400±430 (23.0±3.0)
LS-2	τ_{31}	5480±515 (37.8±3.5)
LS-2	τ_{32}	5270±515 (36.3±3.5)
TS-1	τ_{31}	6050±250 (41.7±1.7)
TS-1	τ_{32}	4095±330 (28.2±2.3)
TS-2	τ_{31}	5905±270 (40.7±1.9)
TS-2	τ_{32}	3510±450 (24.2±3.1)

Table 22 - Interlaminar Shear Strength Data from 0.25" Panels Normalized to 60% Fiber Volume Fraction

Architecture	Shear Strength Tested	Measured Shear Strength psi (MPa)
LS-1	τ_{31}	4390 (30.2)
LS-1	τ_{32}	3530 (24.3)
LS-2	τ_{31}	5450 (37.6)
LS-2	τ_{32}	5210 (35.9)
LS-3	τ_{31}	3890 (26.8)
LS-3	τ_{32}	3425 (23.6)
TS-1	τ_{31}	5980 (41.2)
TS-1	τ_{32}	4030 (27.8)
TS-2	τ_{31}	6100 (42.0)
TS-2	τ_{32}	3630 (25.0)
TS-3	τ_{31}	4115 (28.4)
TS-3	τ_{32}	3690 (25.4)
OS-3	τ_{31}	4735 (32.6)
OS-3	τ_{32}	5450 (37.6)

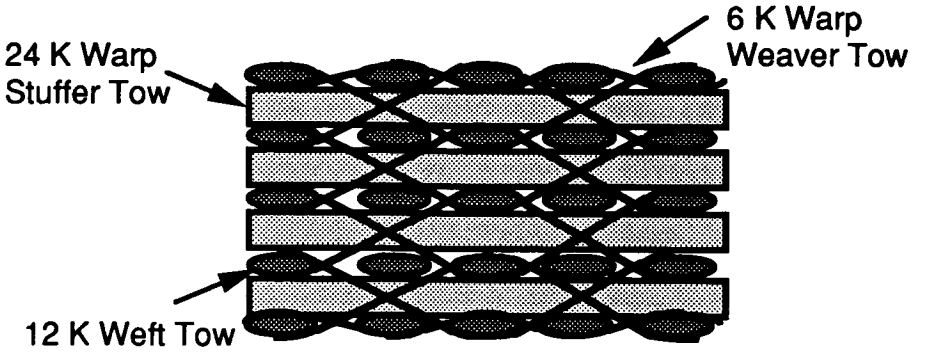

(a) LS-1

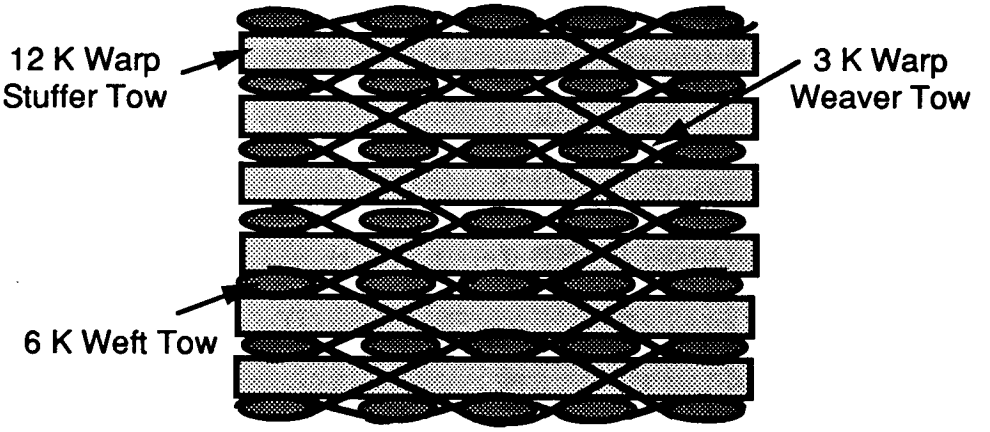

(b) LS-2

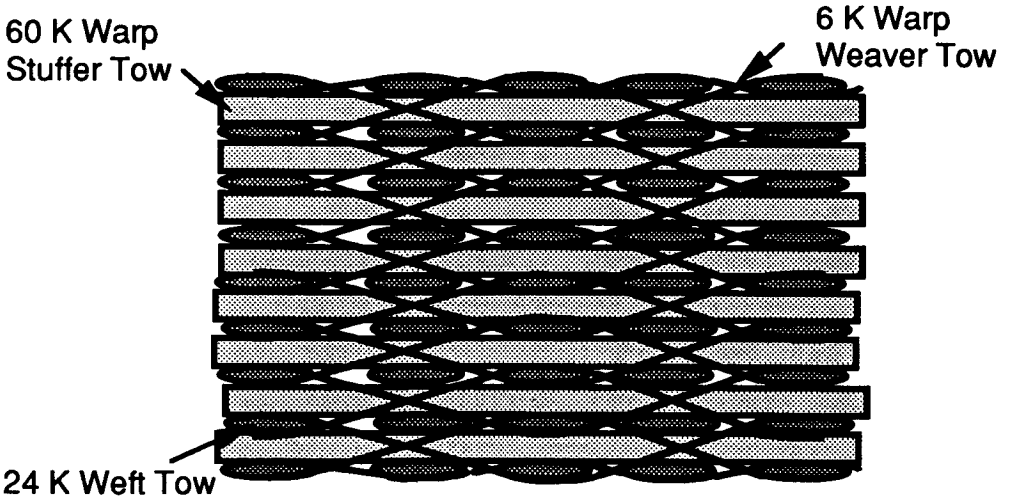

(c) LS-3

Figure 1 - Schematics of layer-to-layer angle interlock preform architectures

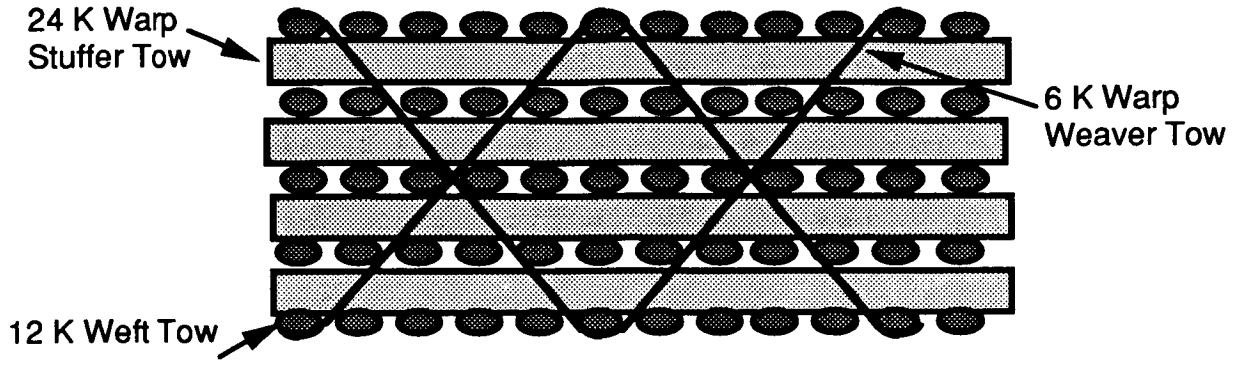

(a) TS-1

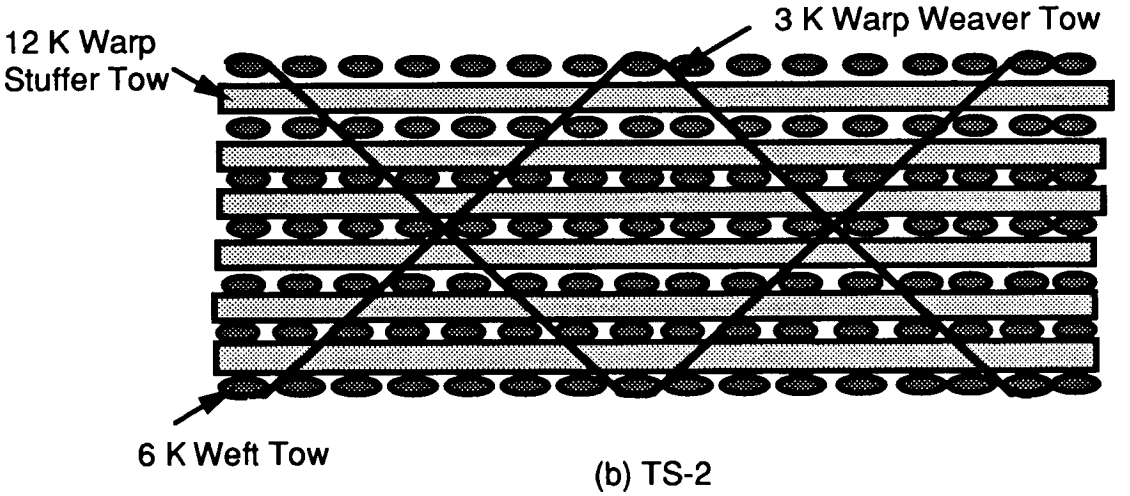

(b) TS-2

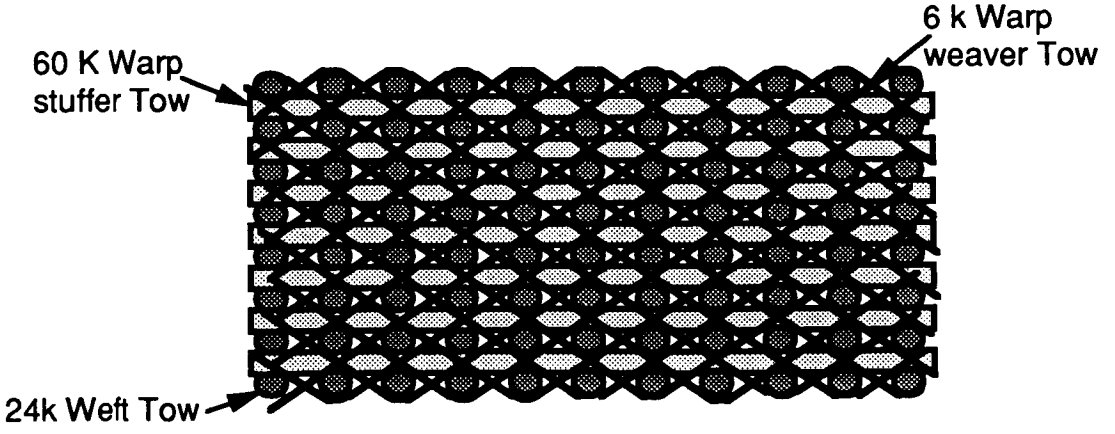

(c) TS-3

Figure 2 - Schematics of throught-the-thickness angle interlock architectures

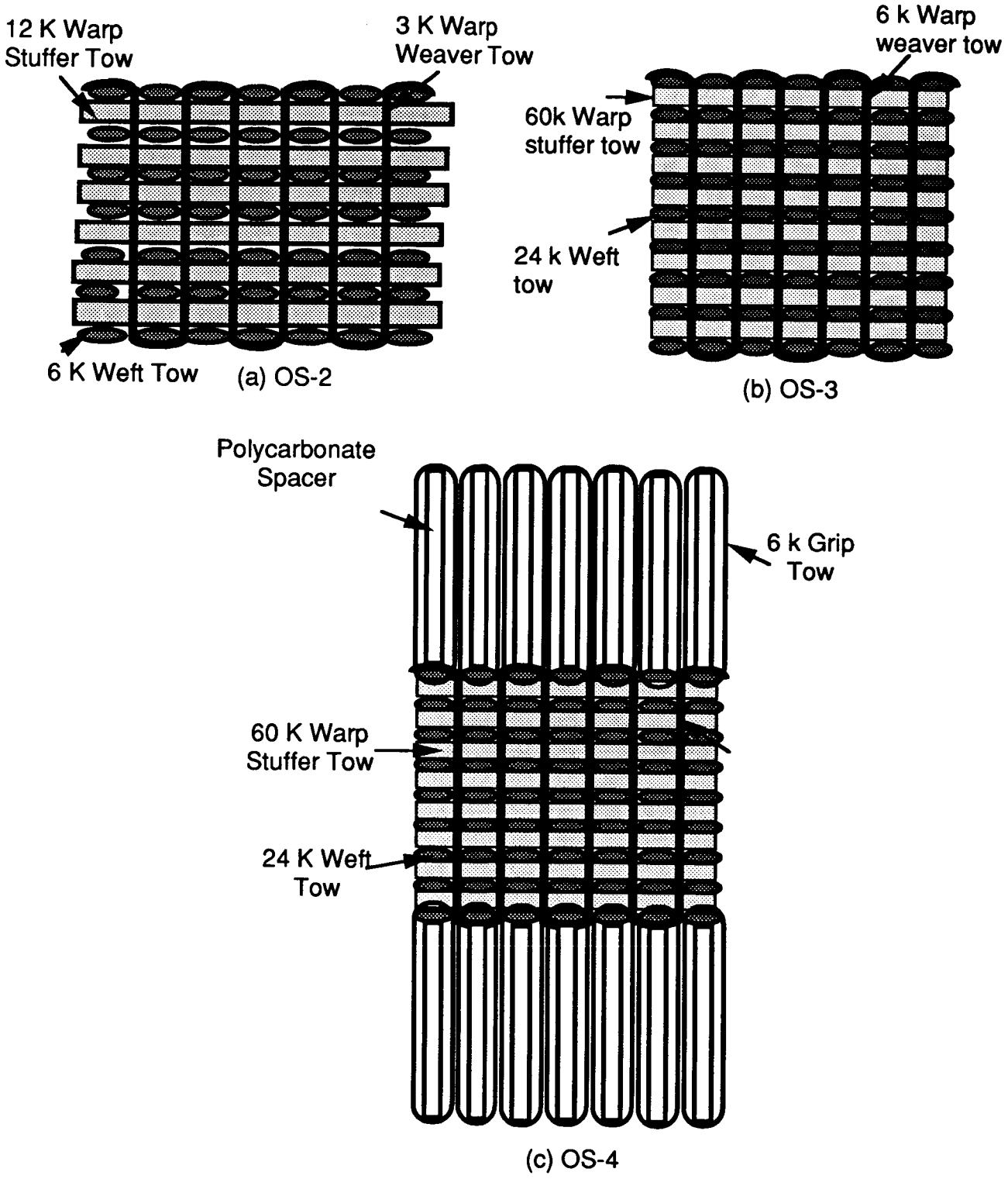

Figure 3 - Schematics of through-the-thickness orthogonal weave architectures

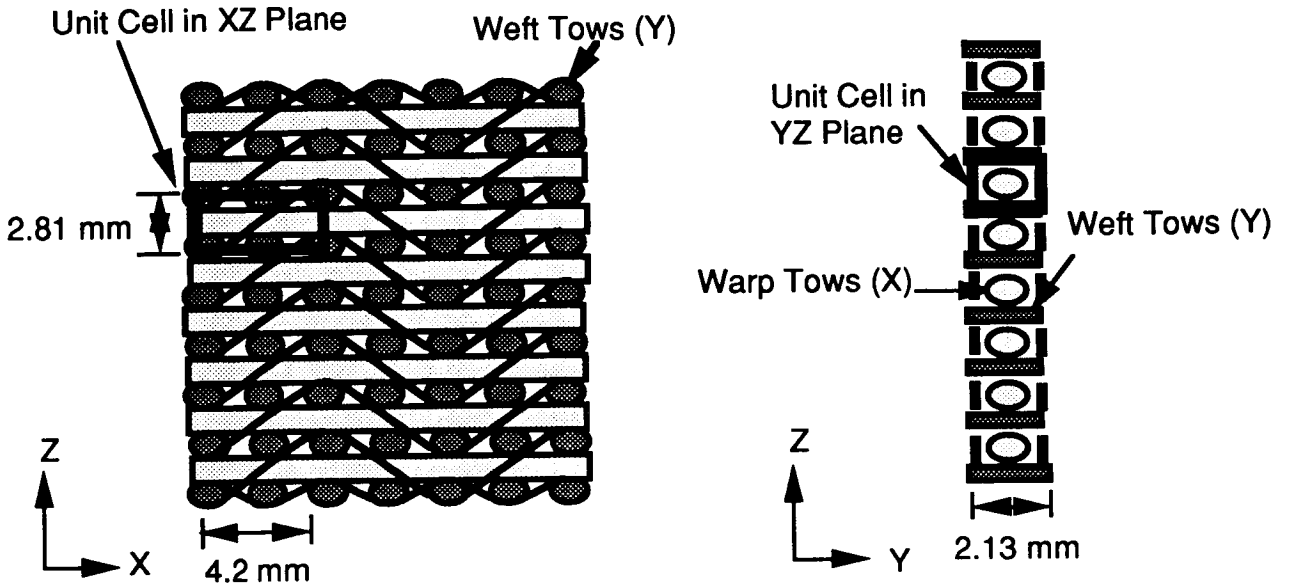

(a)

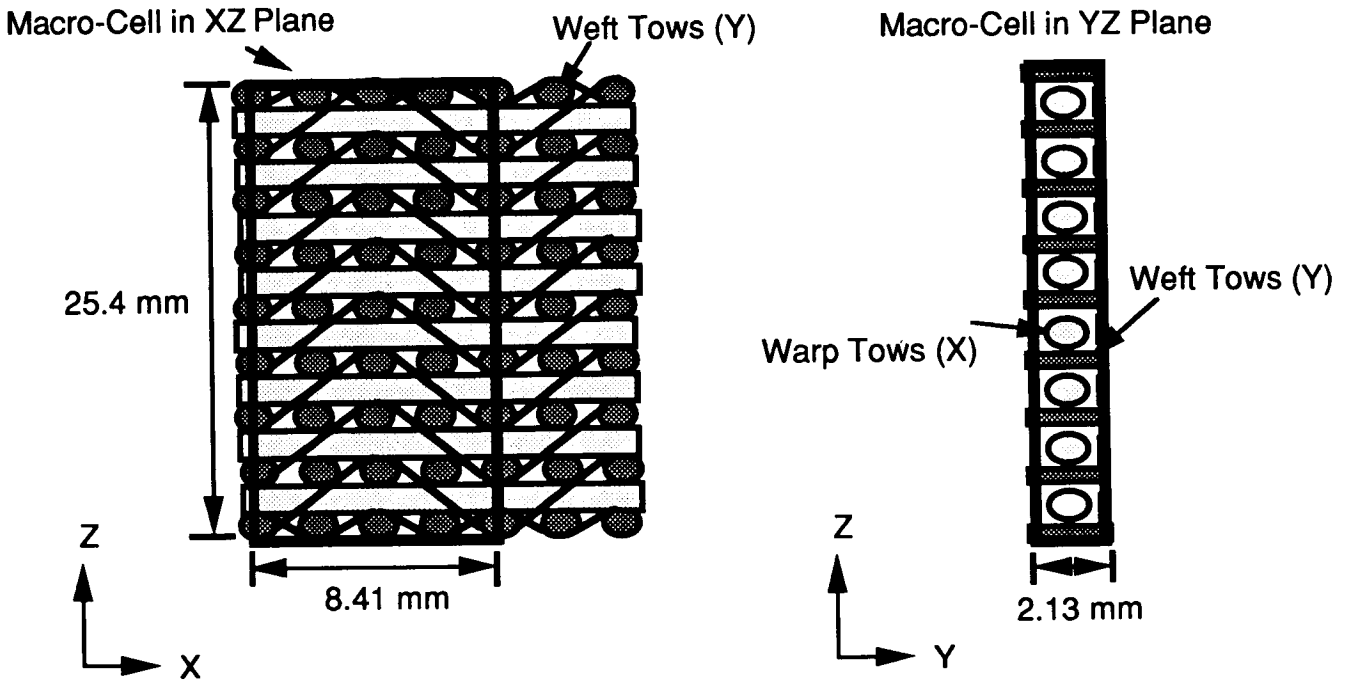

(b)

Figure 4 - Schematics of (a) a unit cell and (b) a macro-cell for a LS-3 architecture.

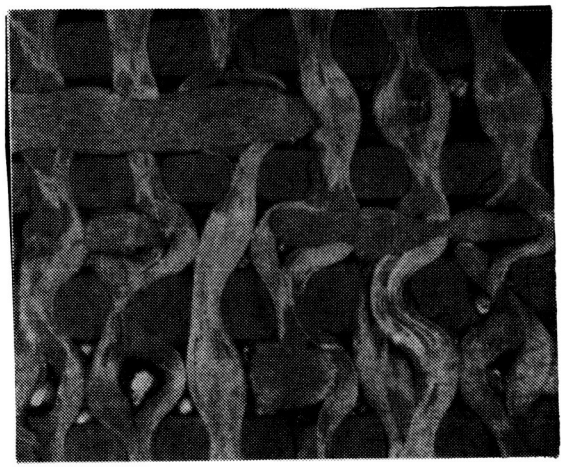

(a)

(b)

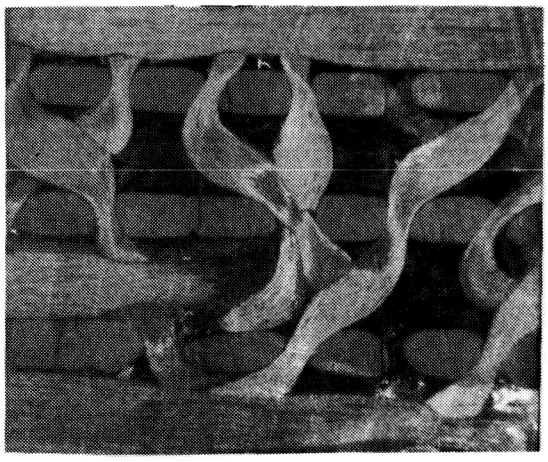

(c)

Figure 5 - Examples of RTM-induced tow distortions for (a) OS-3 composite, (b) LS-3 composite, and (c) TS-3 composite.

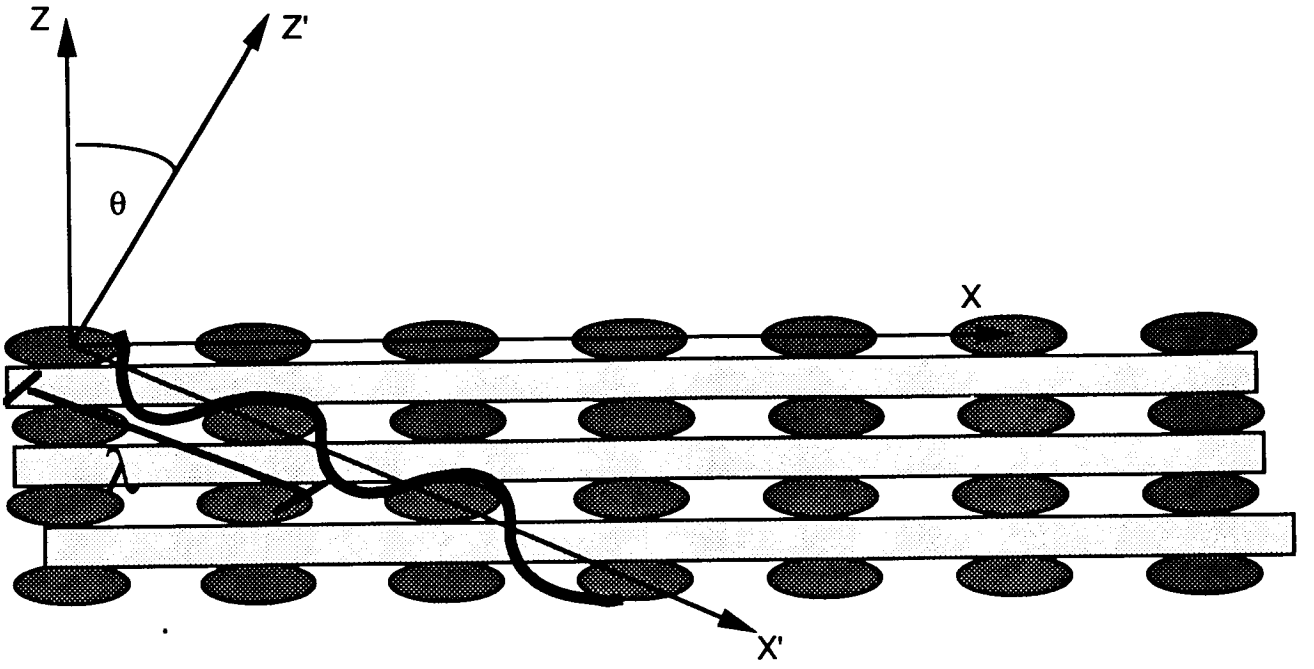

Undulation aprroximated by sinusodial path

$$Z' = A \cdot \sin\left(\frac{2\pi X'}{\lambda}\right)$$

Figure 6 - Simplified model of distorted warp weaver tow.

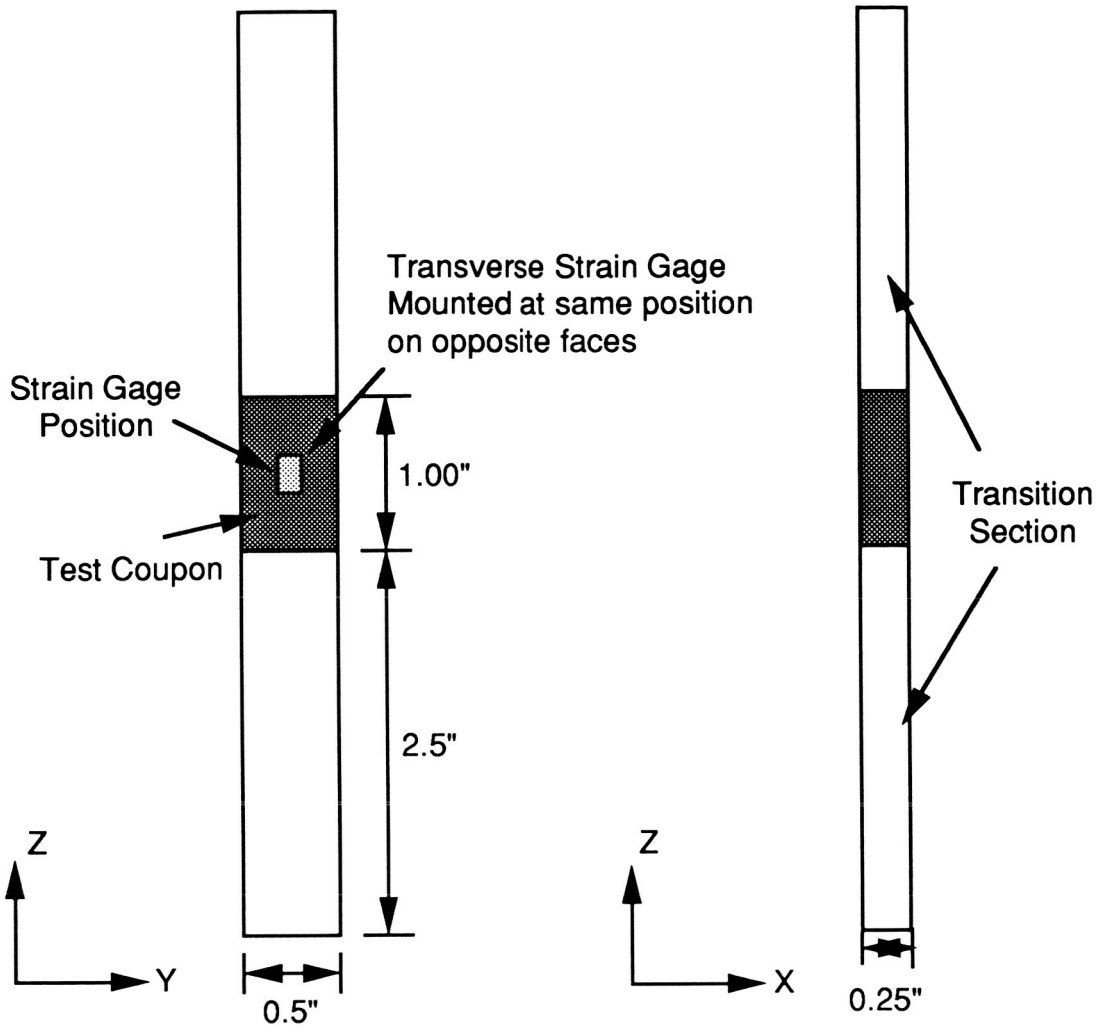

Figure 7 - Dimensions of Generation 2 bi-material tensile specimen.

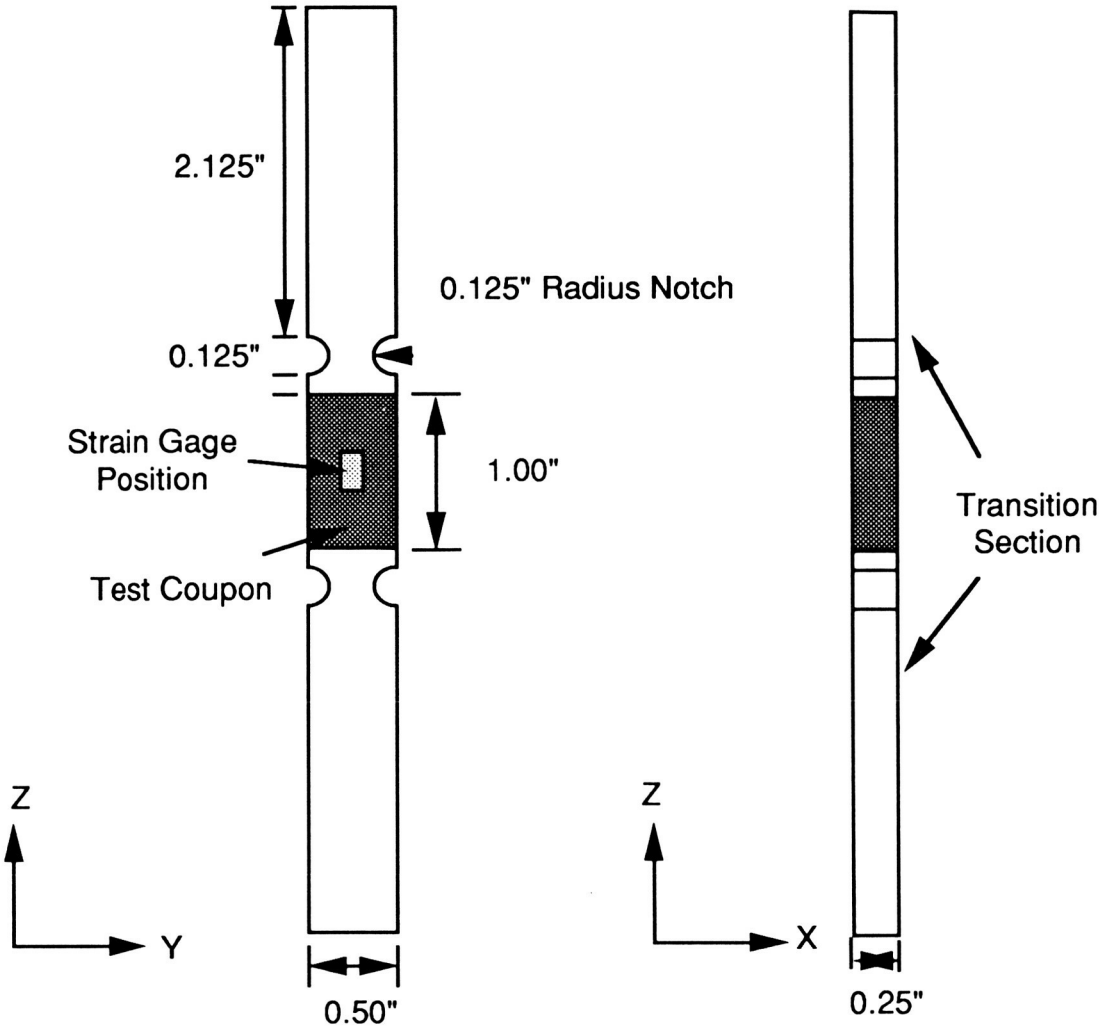

Figure 8 - Dimensions of Generation 3 bi-material tensile specimen.

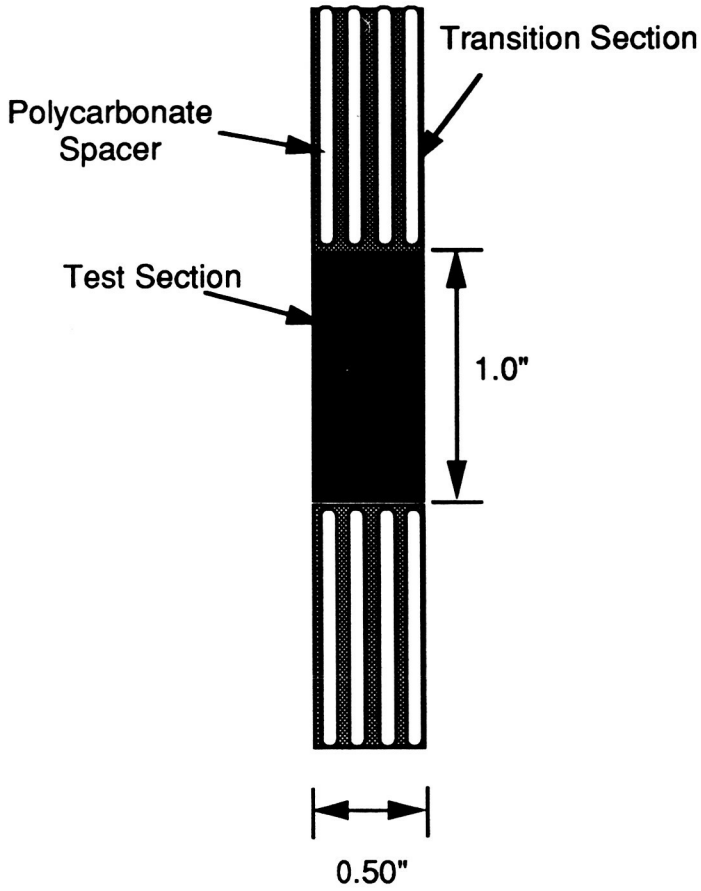

Figure 9 - Schematic of the integrated-grid tensile specimen using the OS-4 architecture.

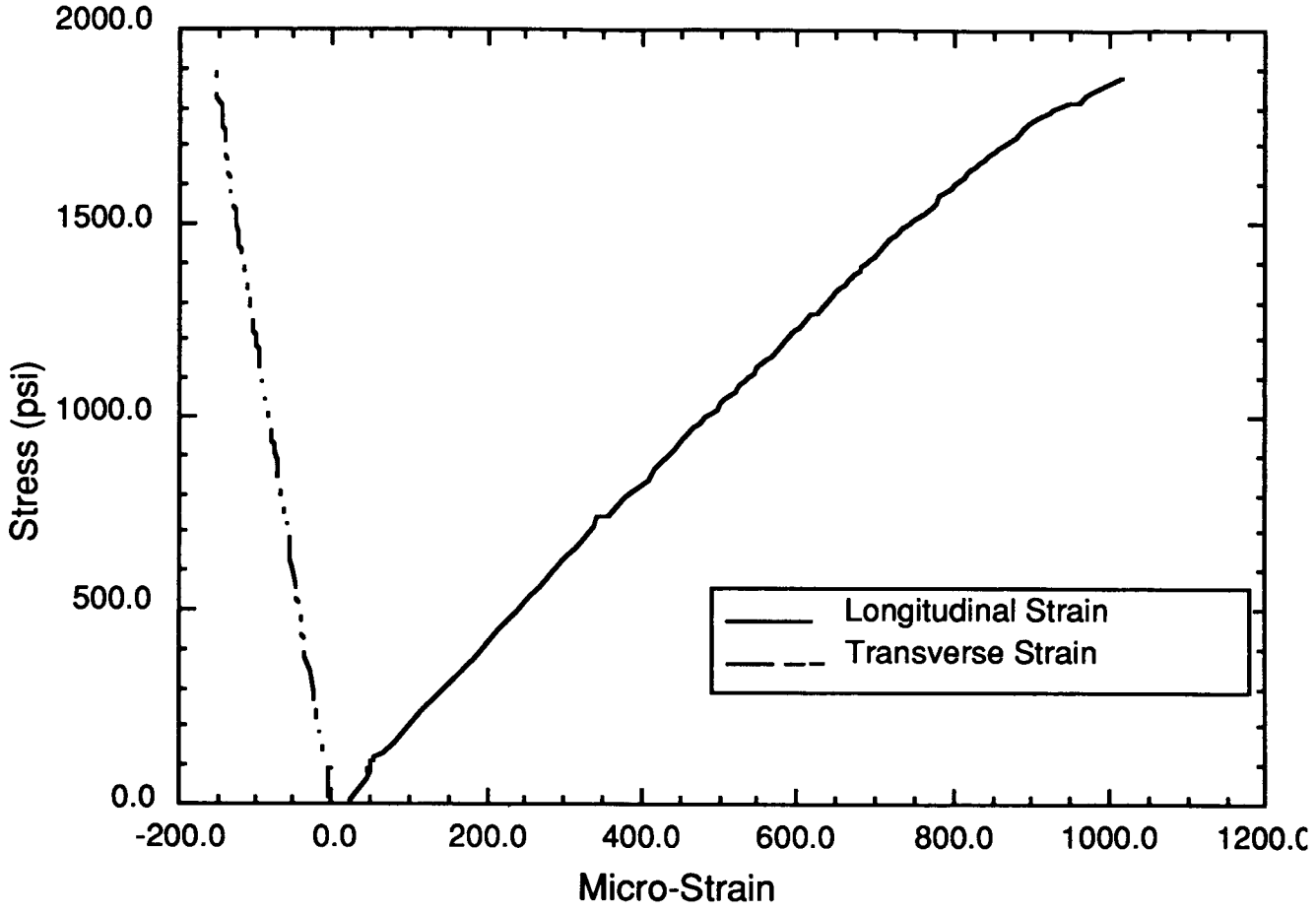

Figure 10 - Typical tensile stress-strain curve for generation 3 specimens of TS-3 composite

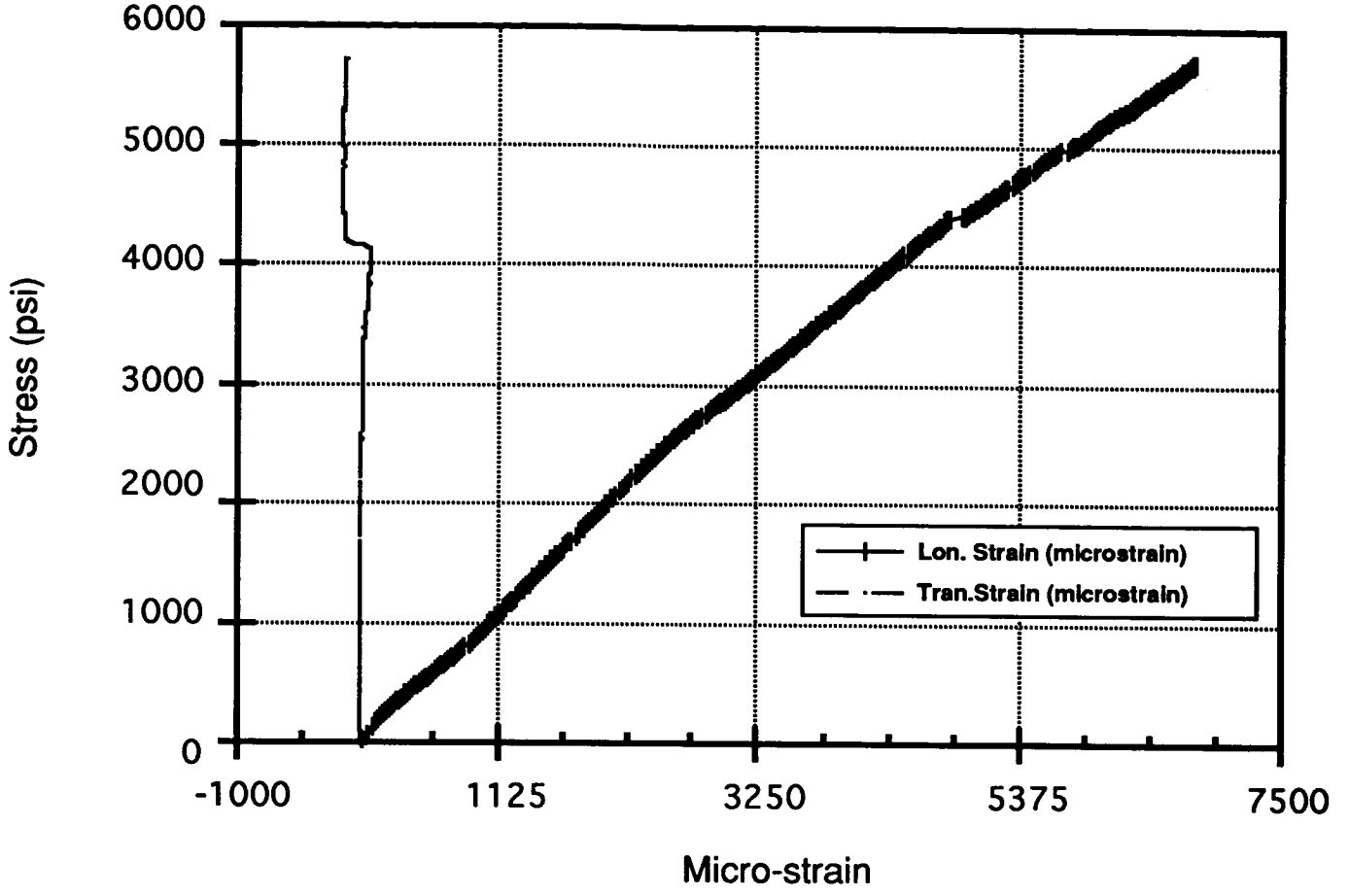

Figure 11 - Typical tensile stress-strain plot for OS-4 integrated-grip specimen.

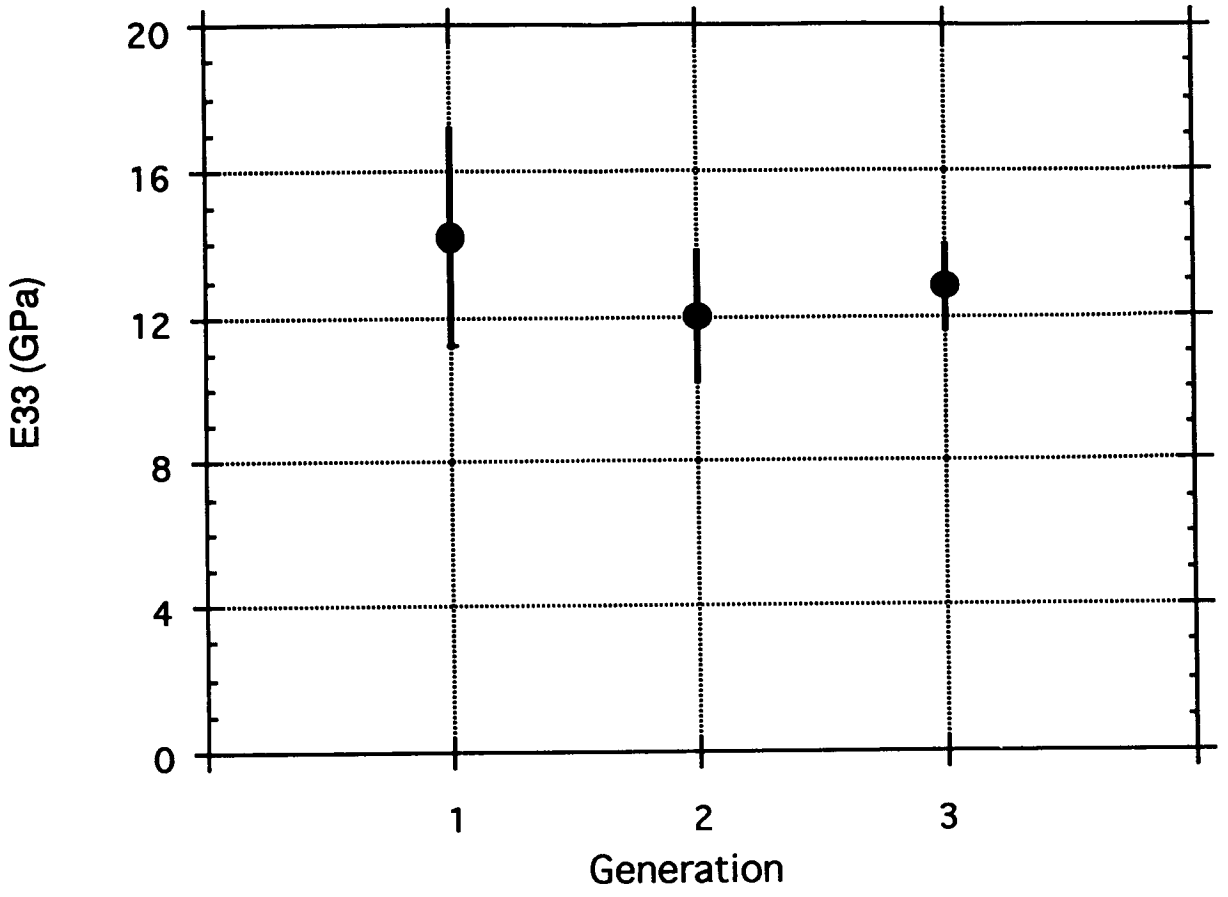

Figure 12 - Improvement in data reproducibility with specimen generation.

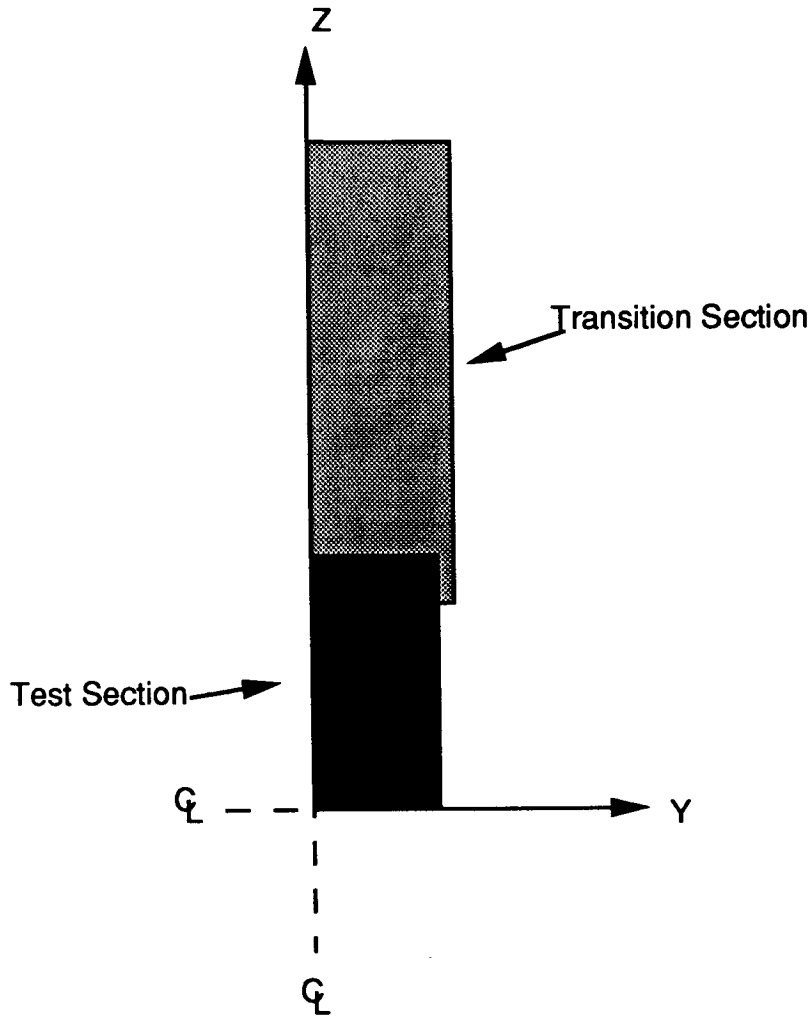

Figure 13 - Quarter schematic of proposed lap-joint specimen configuration.

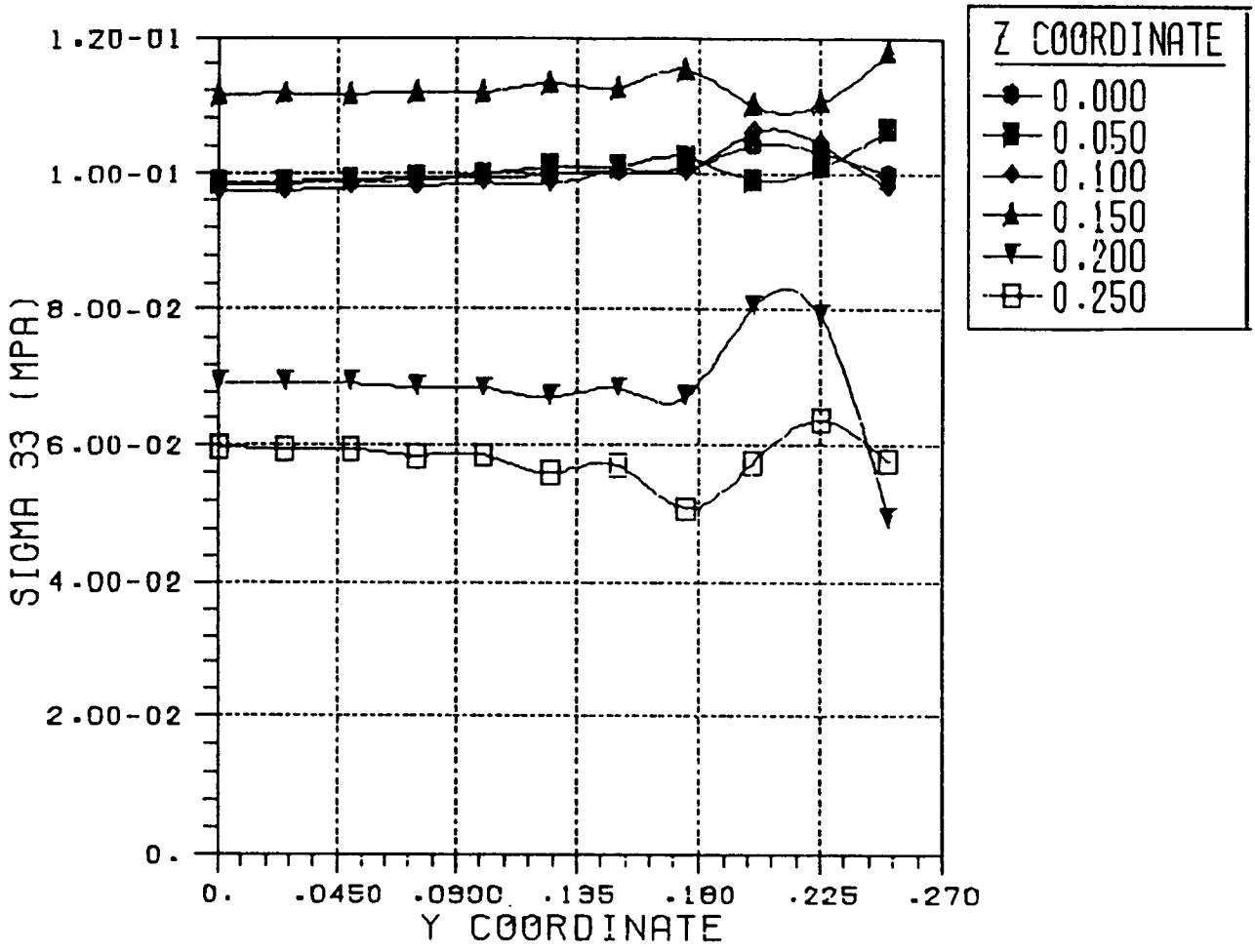

Figure 14 - Predicted through-the-thickness tensile stress field for lap-joint specimen configuration.

Figure 15 - Proposed integrated-grip dogbone tensile specimen.

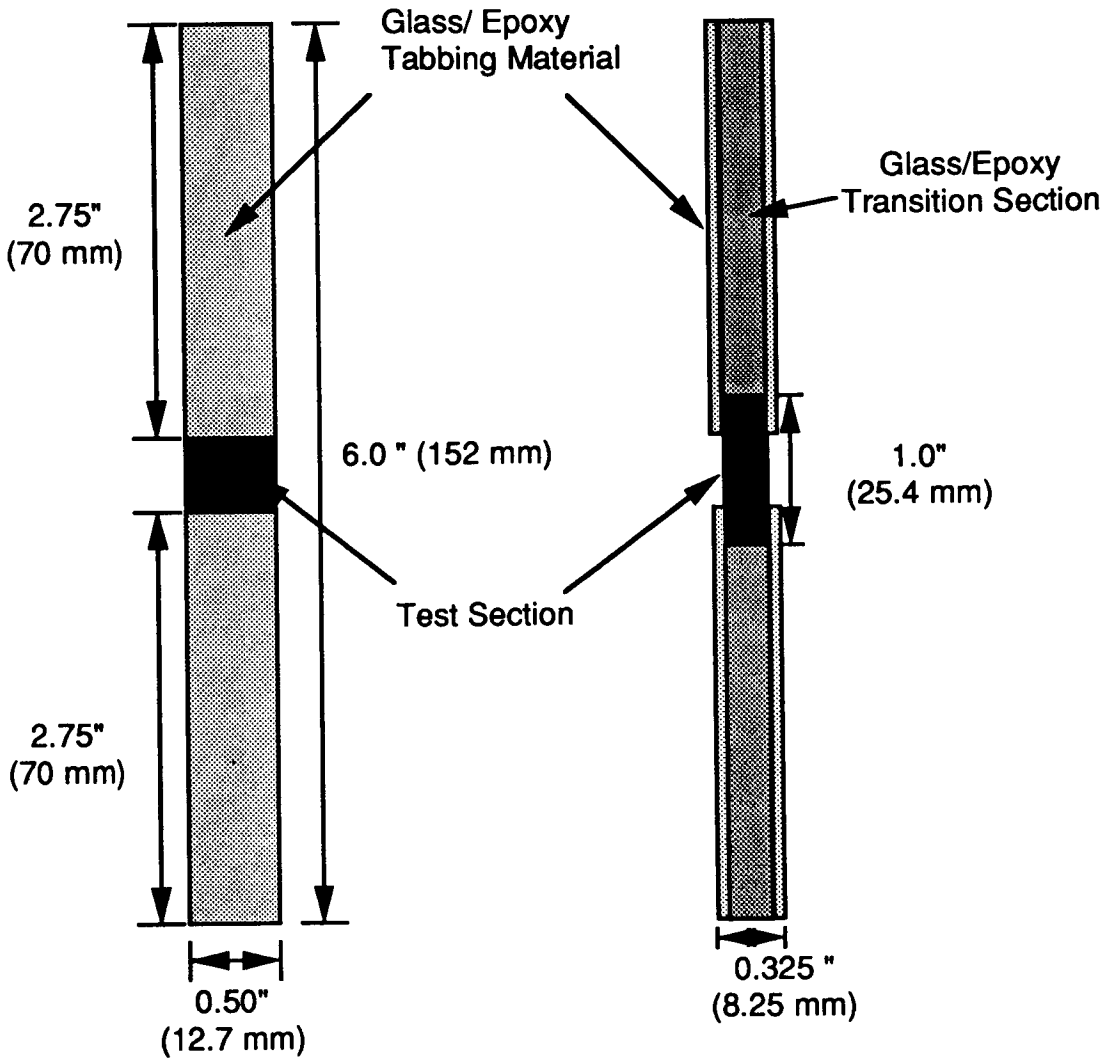

Figure 16 - Schematic of through-the-thickness compression specimen.

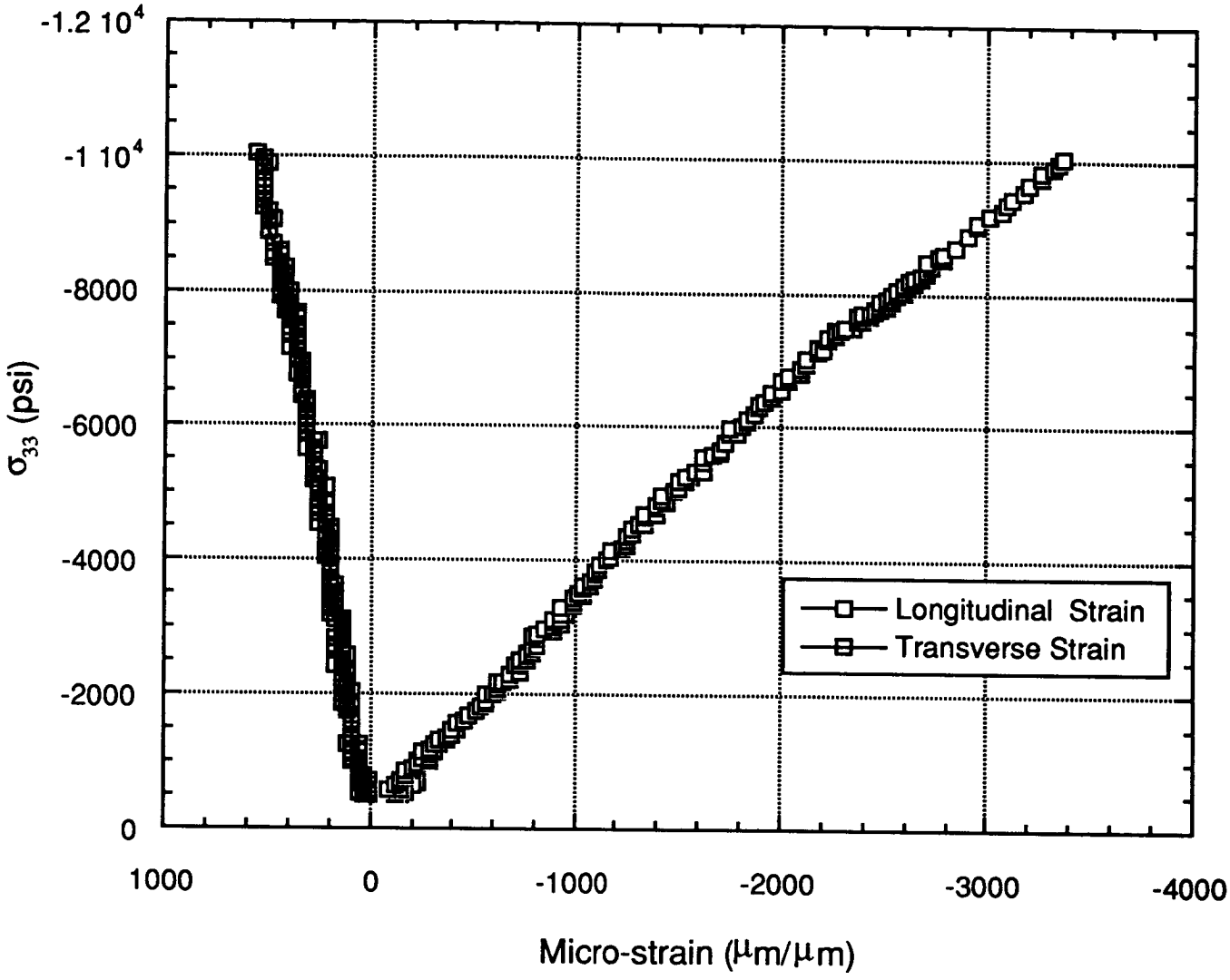

Figure 17 - Typical compressive stress-strain curve for OS-3 composite.

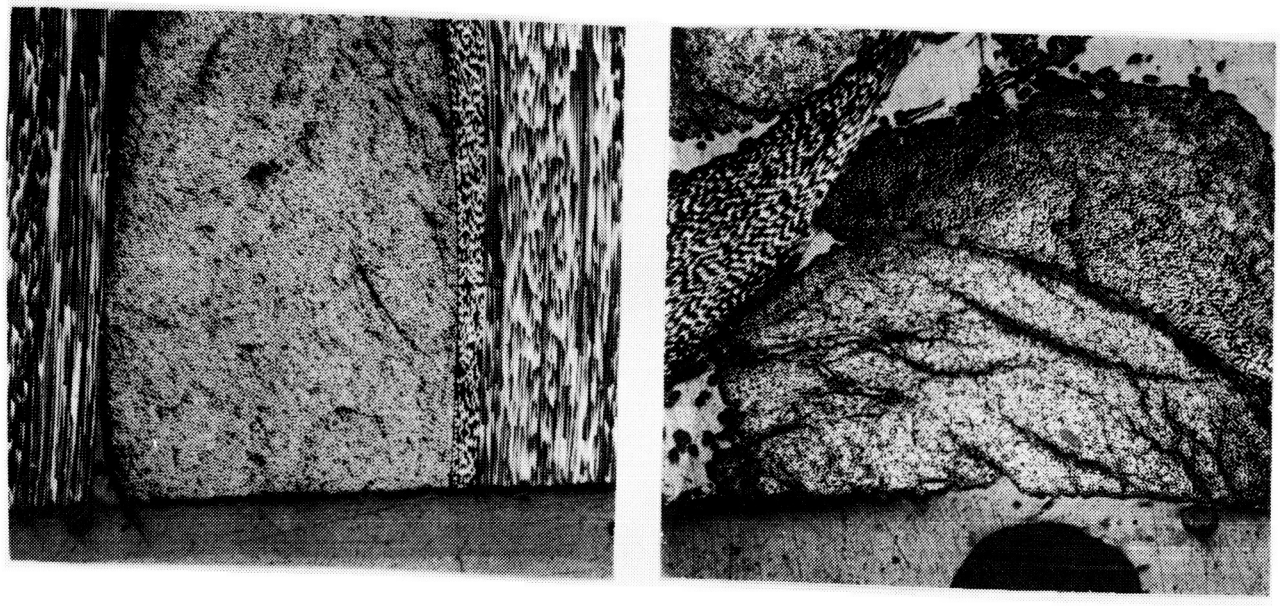

(a) (b)

(c) (d)

Figure 18 - Compressive damage progression in the surface weft tows of LS-3 specimen loaded to (a) 110 MPa, (b) 165 MPa, (c) 220 MPa and (d) Peak Load.

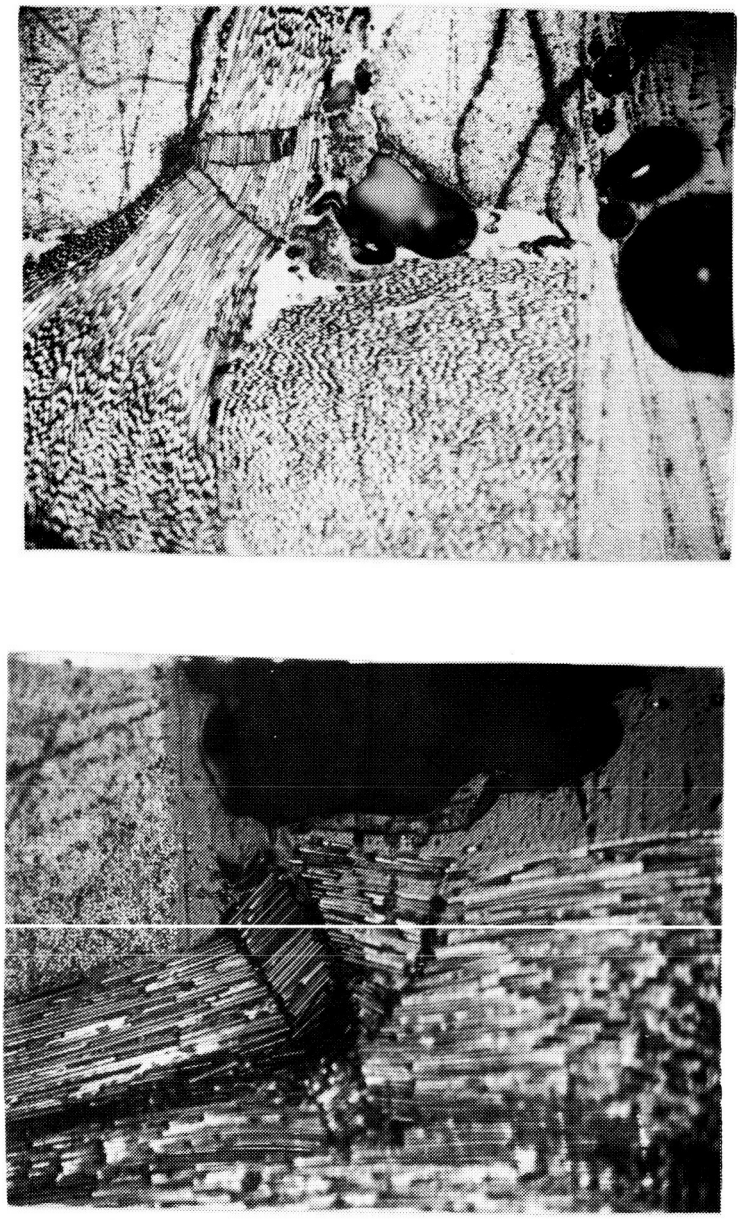

Figure 19 - Examples of kink bands near voids.

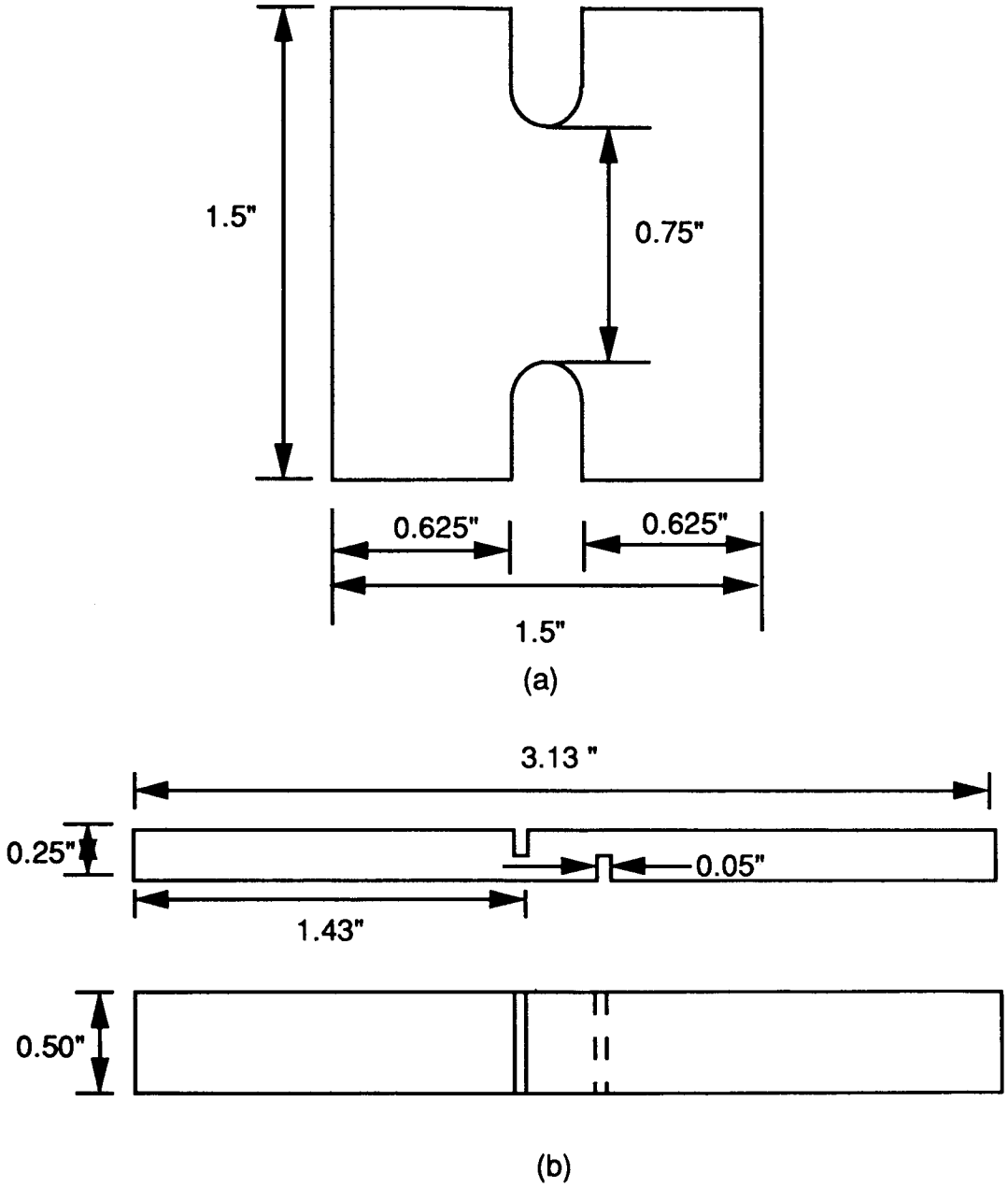

Figure 20 - Schematics of (a) baseline Compact Shear (CS) specimnen, and (b) Standard ASTM D3846-79 Double Notch Shear (DNS) specimen.

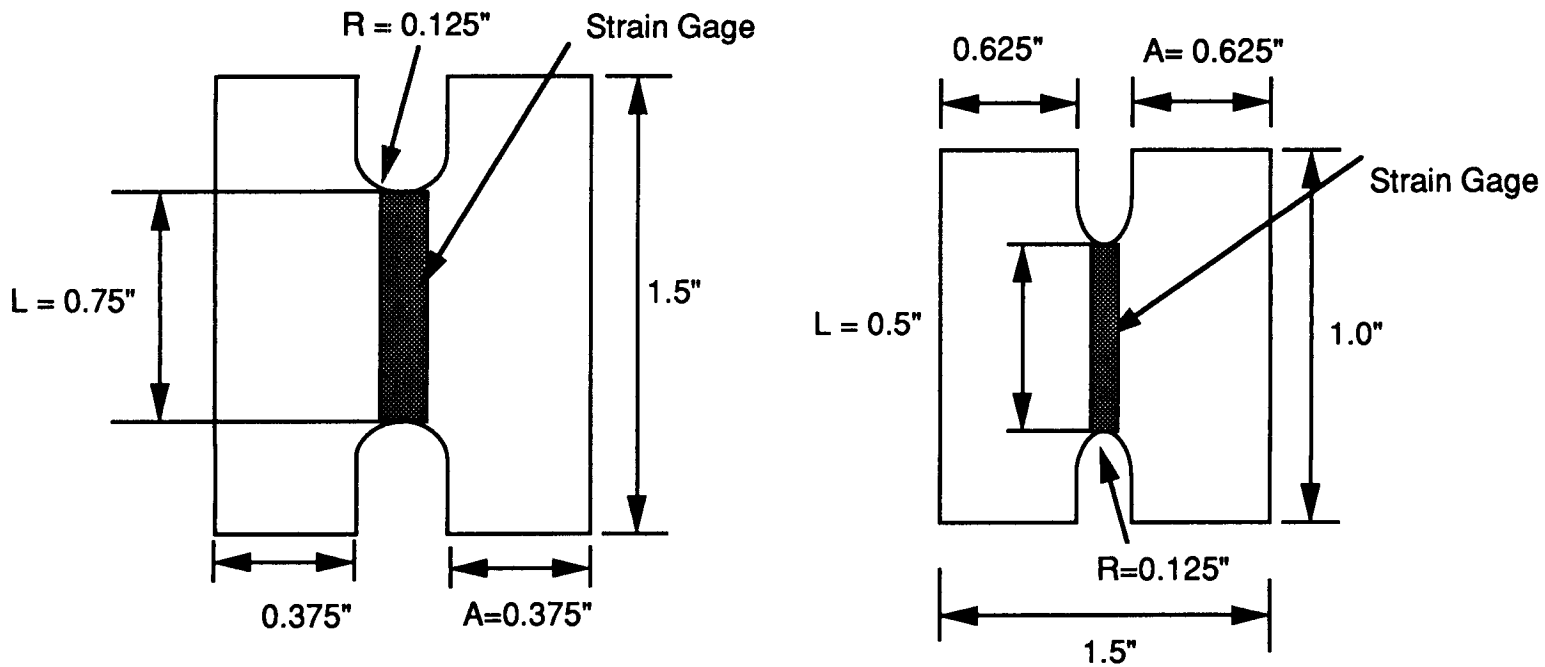

(a) TTIS1

(b) TTIS2

Figure 21 - Schematics of the two modified CS specimens for (a) interlaminar (TTIS1) and (b) transverse(TTIS2) shear testing.

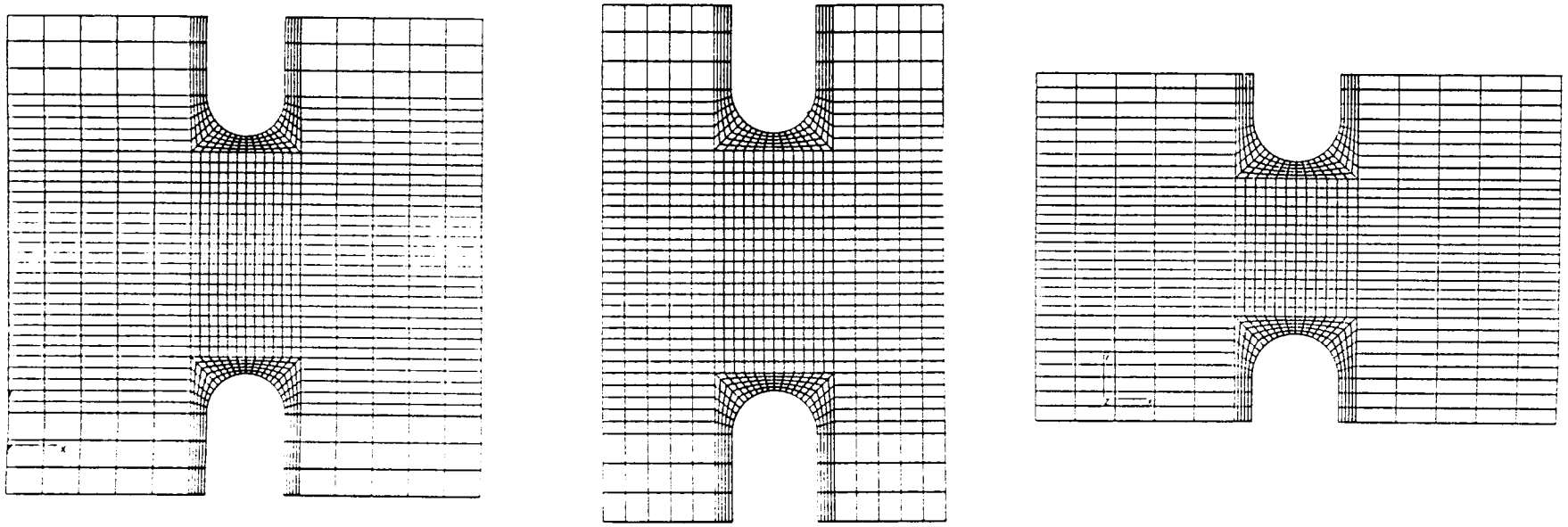

(a) (b) (c)

Figure 22 - FEM meshes for (a) baseline CS, (b) TTIS1, and (c) TTIS2 specimens.

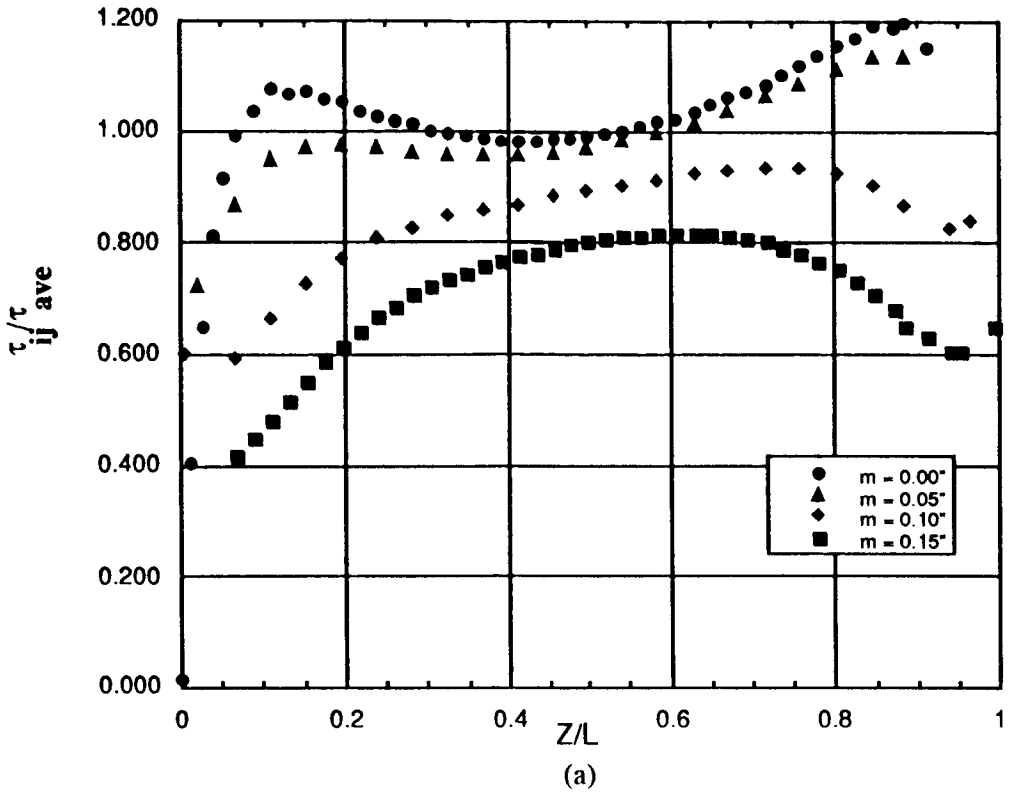

(a)

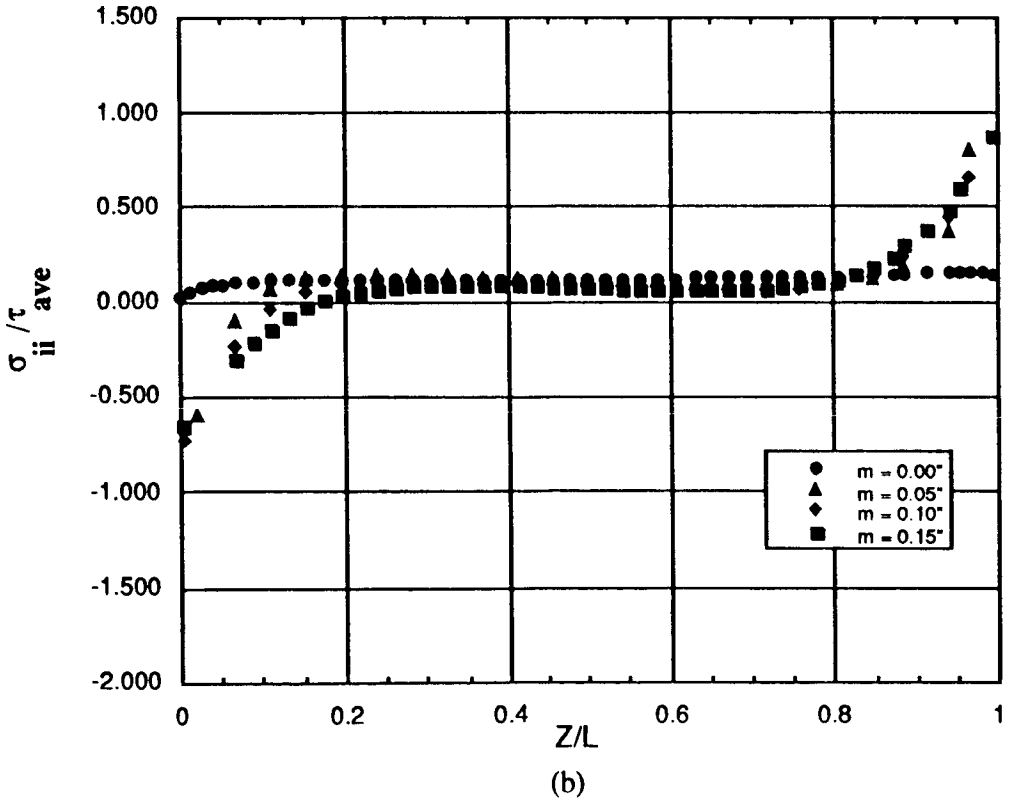

(b)

Figure 23 - Normalized stress distruibutions from FEM analysis for baseline CS specimen; (a) shear stress (b) transverse tensile stress.

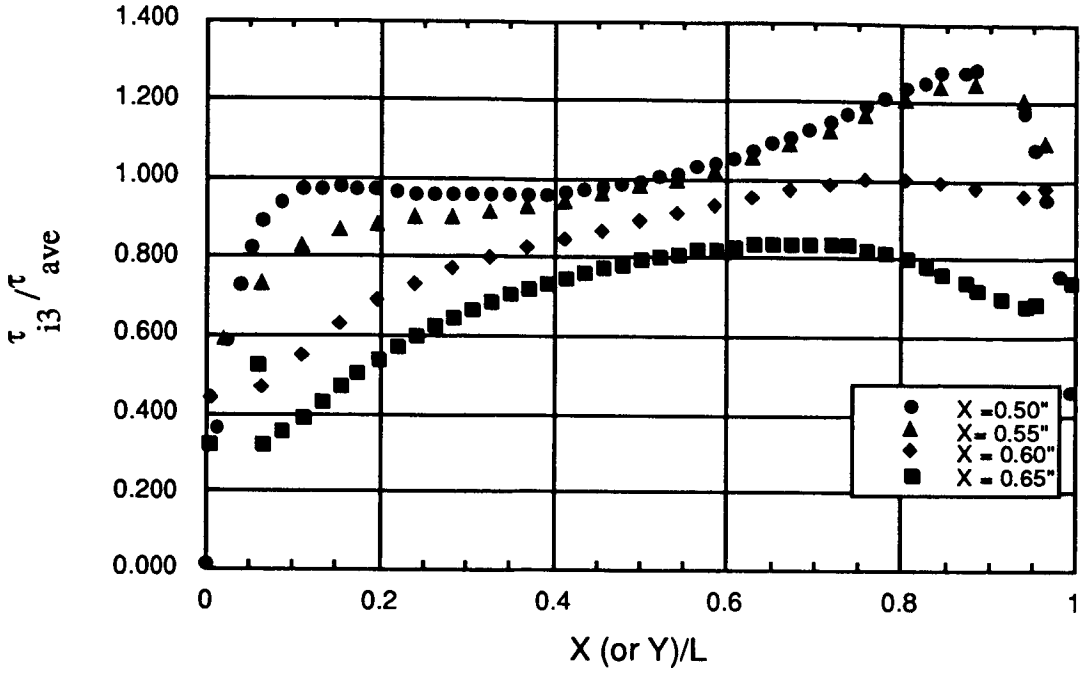

(a)

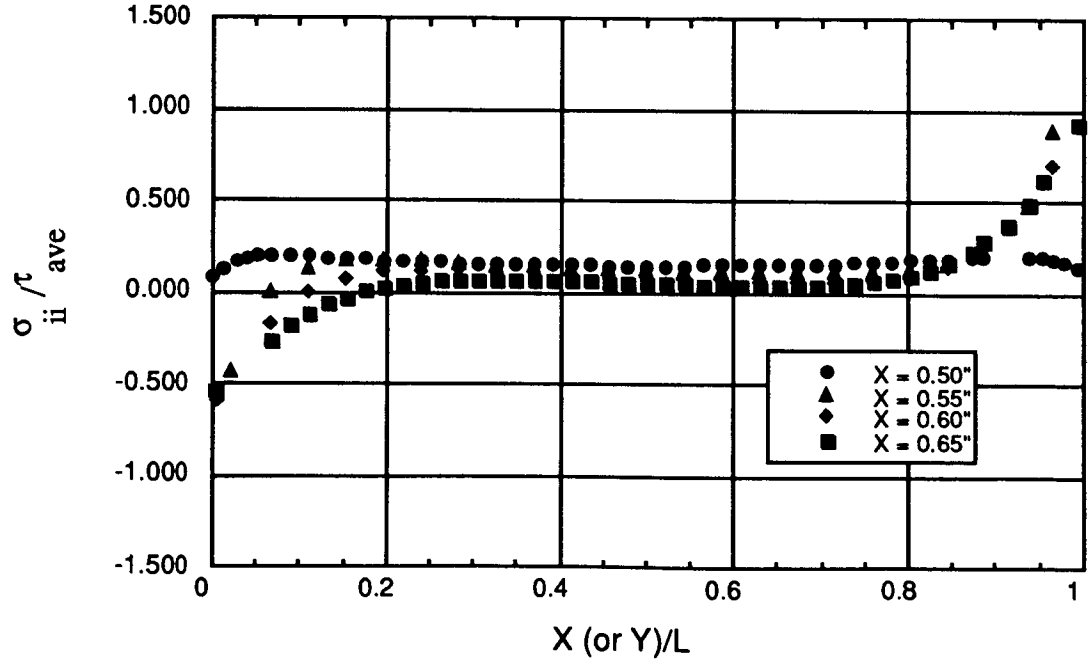

(b)

Figure 24 - Normalized stress distruibutions from FEM analysis for TTIS1 specimen; (a) shear stress (b) transverse tensile stress.

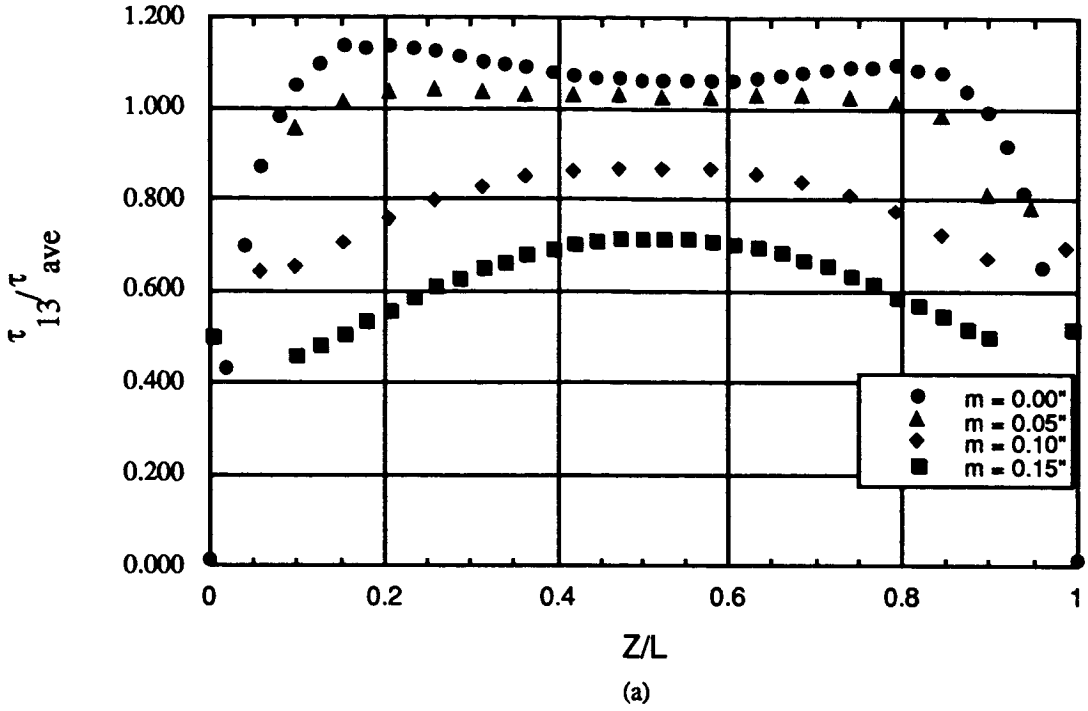

(a)

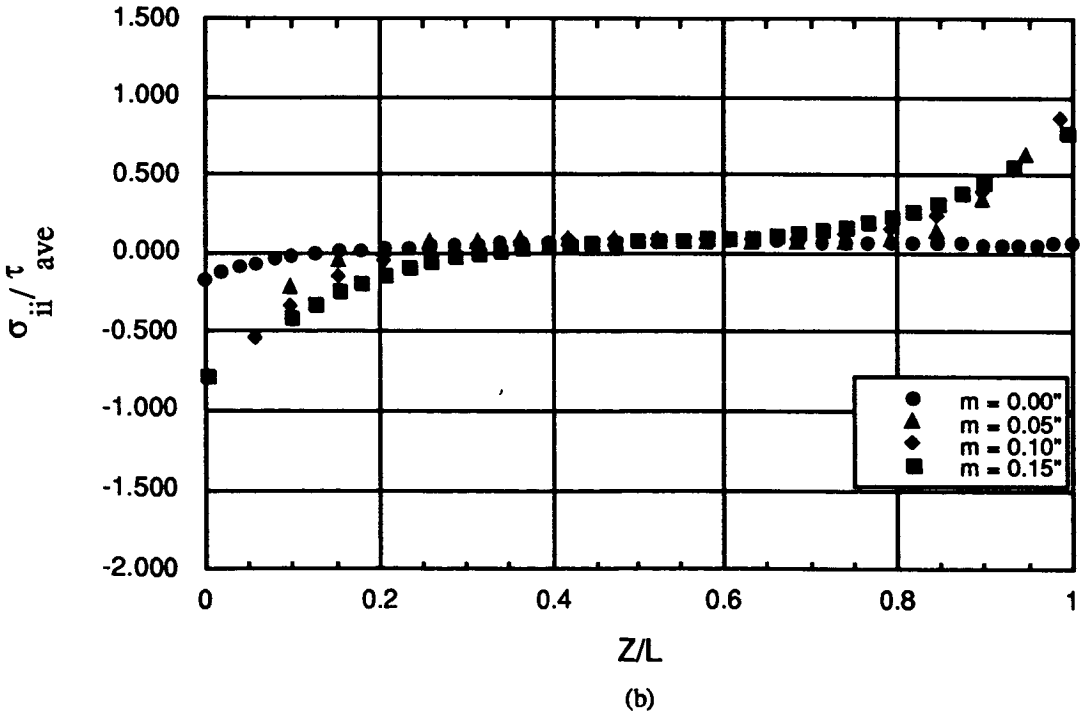

(b)

Figure 25 - Normalized stress distruibutions from FEM analysis for TTIS2 specimen; (a) shear stress and (b) transverse tensile specimen.

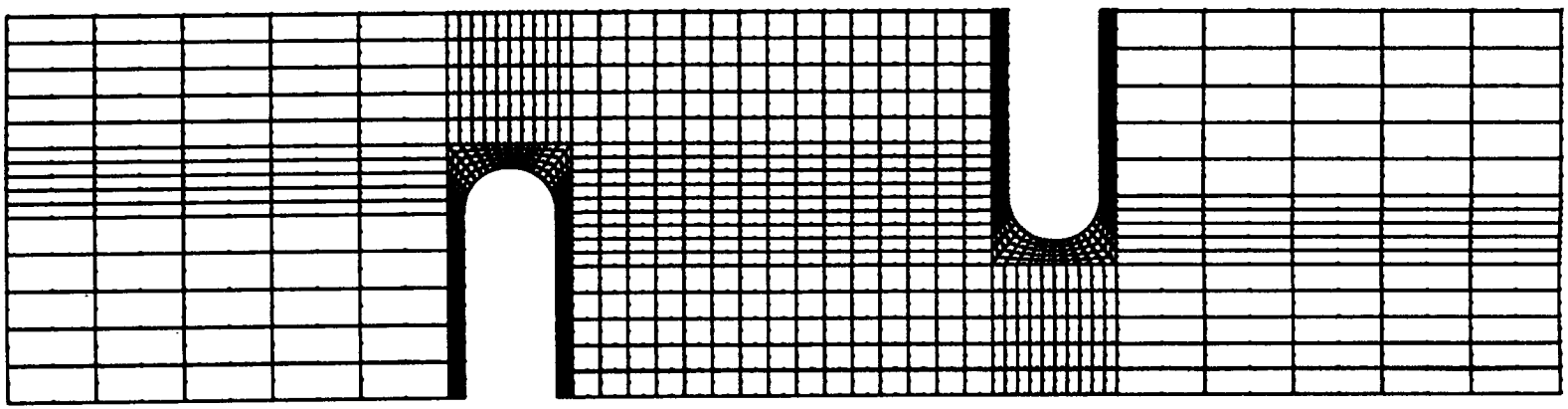

Figure 26 - FEM mesh for the modified DNS specimen.

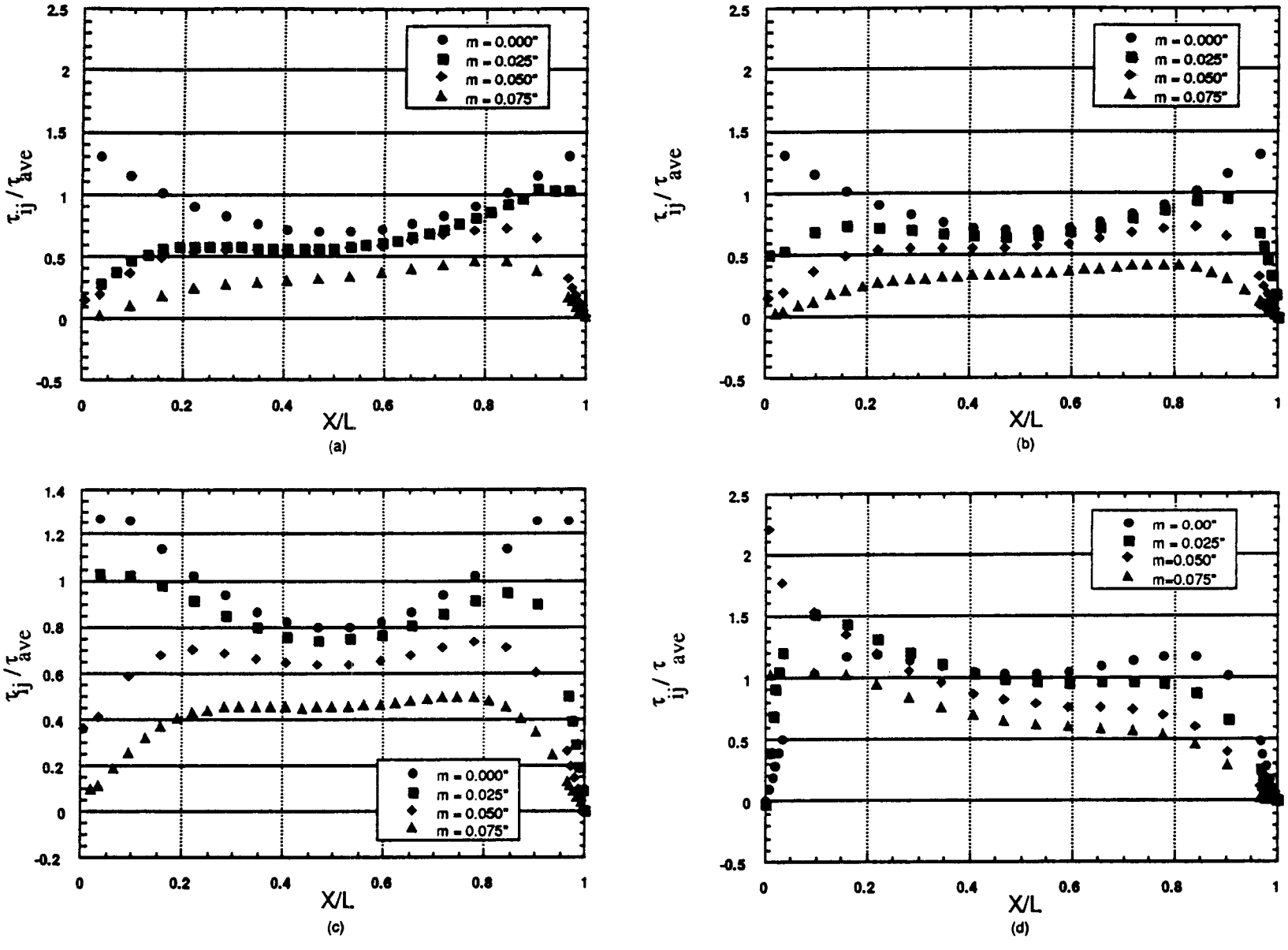

Figure 27 - Normalized shear stress distributions for modified DNS specimen with (a) L=0.290" H=0%, (b) L=0.290" H=10%, (c) L=0.290" H=20%, and (d) L=0.290" H=50%

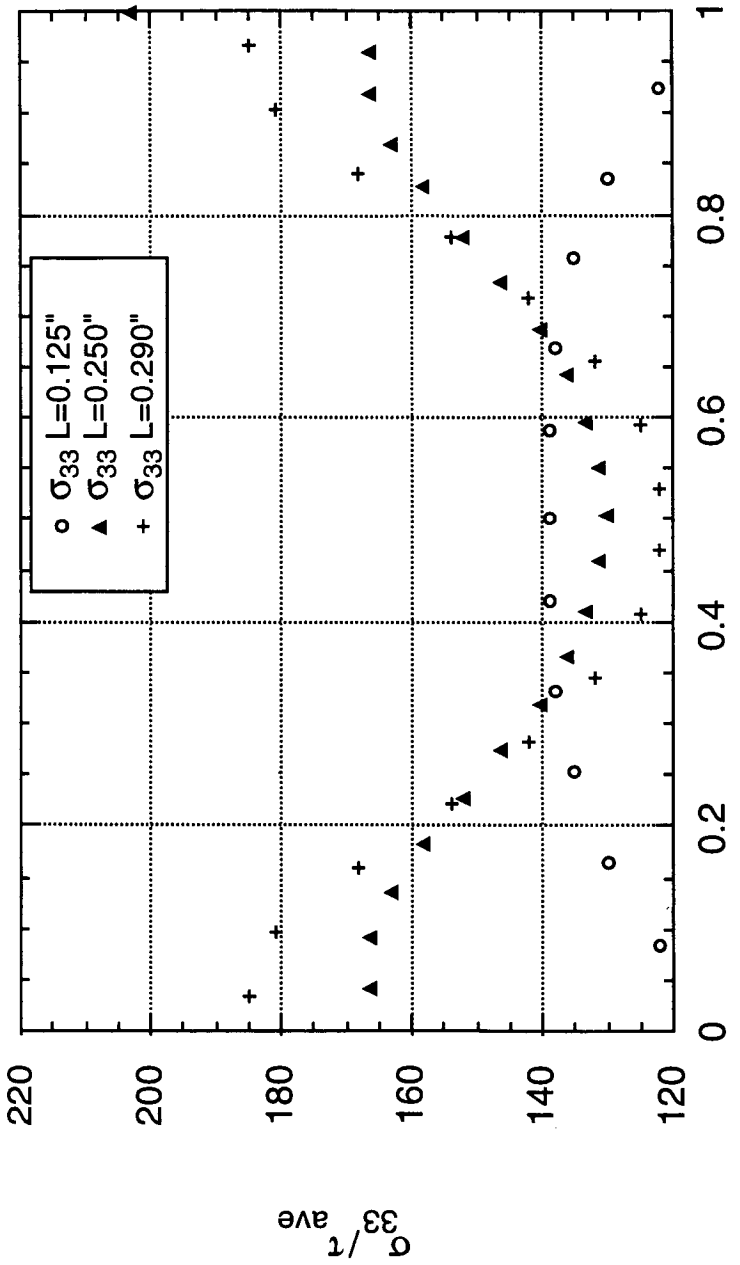

Figure 28 - Transverse tensile stress distributions for modified DNS specimens with H=0% and different L values.

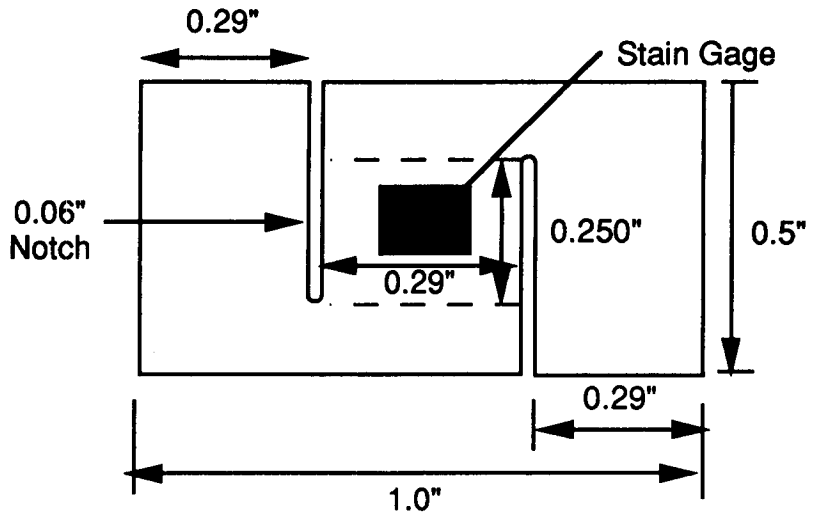

(a)

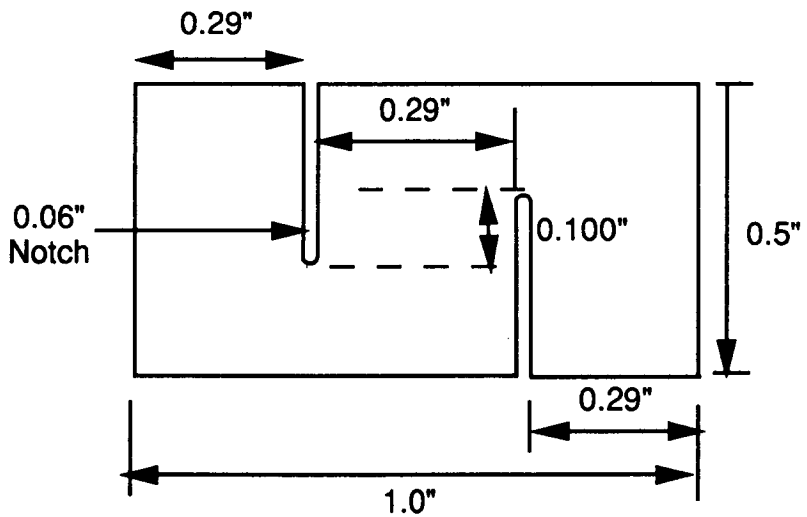

(b)

Figure 29 - Schematics of modified DNS specimens for (a) shear elastic modulus and (b) shear strength measurements.

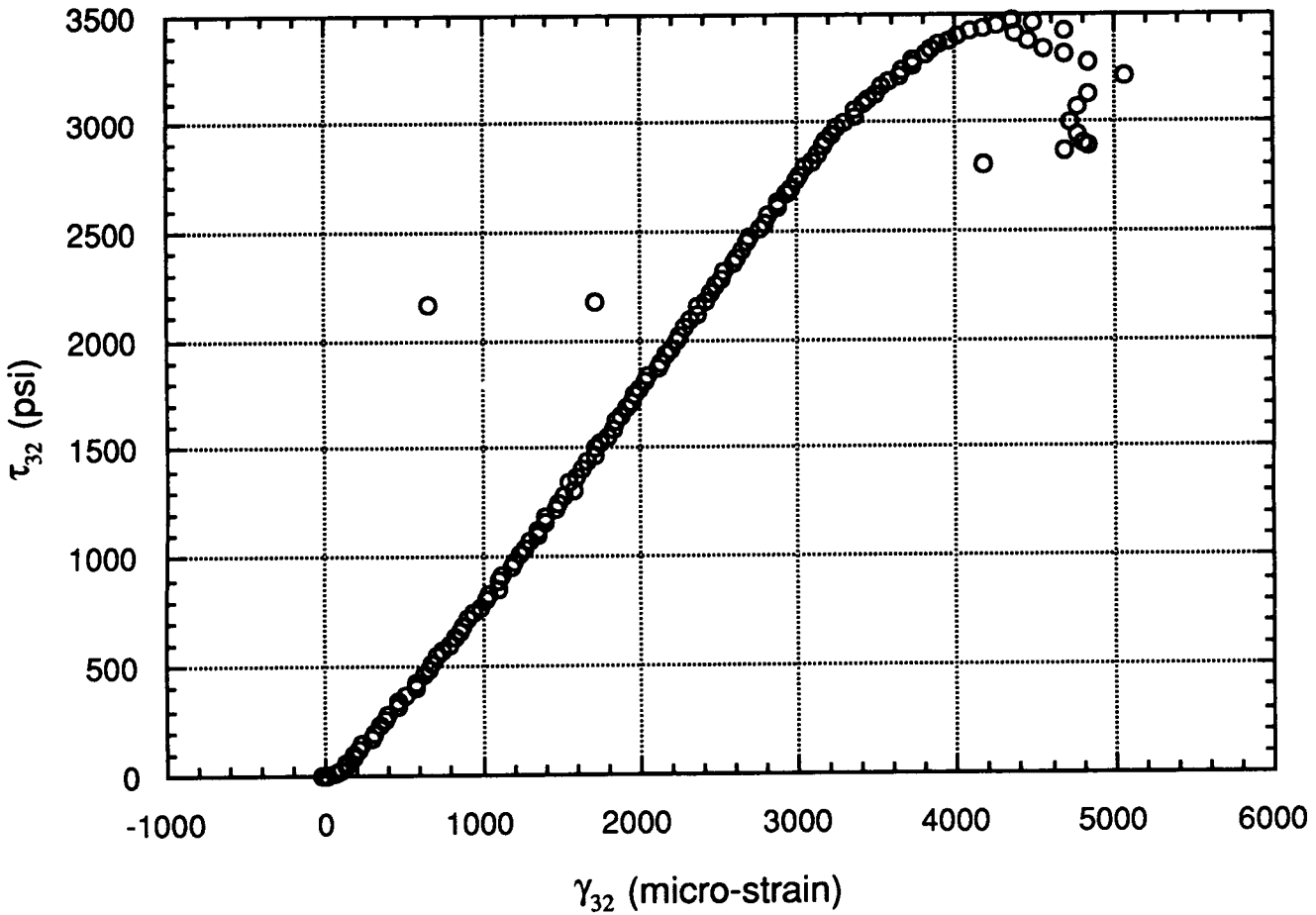

Figure 30 - Shear stress-strain curve obtained for LS-3 composite using modified TTIS1 specimen configuration.

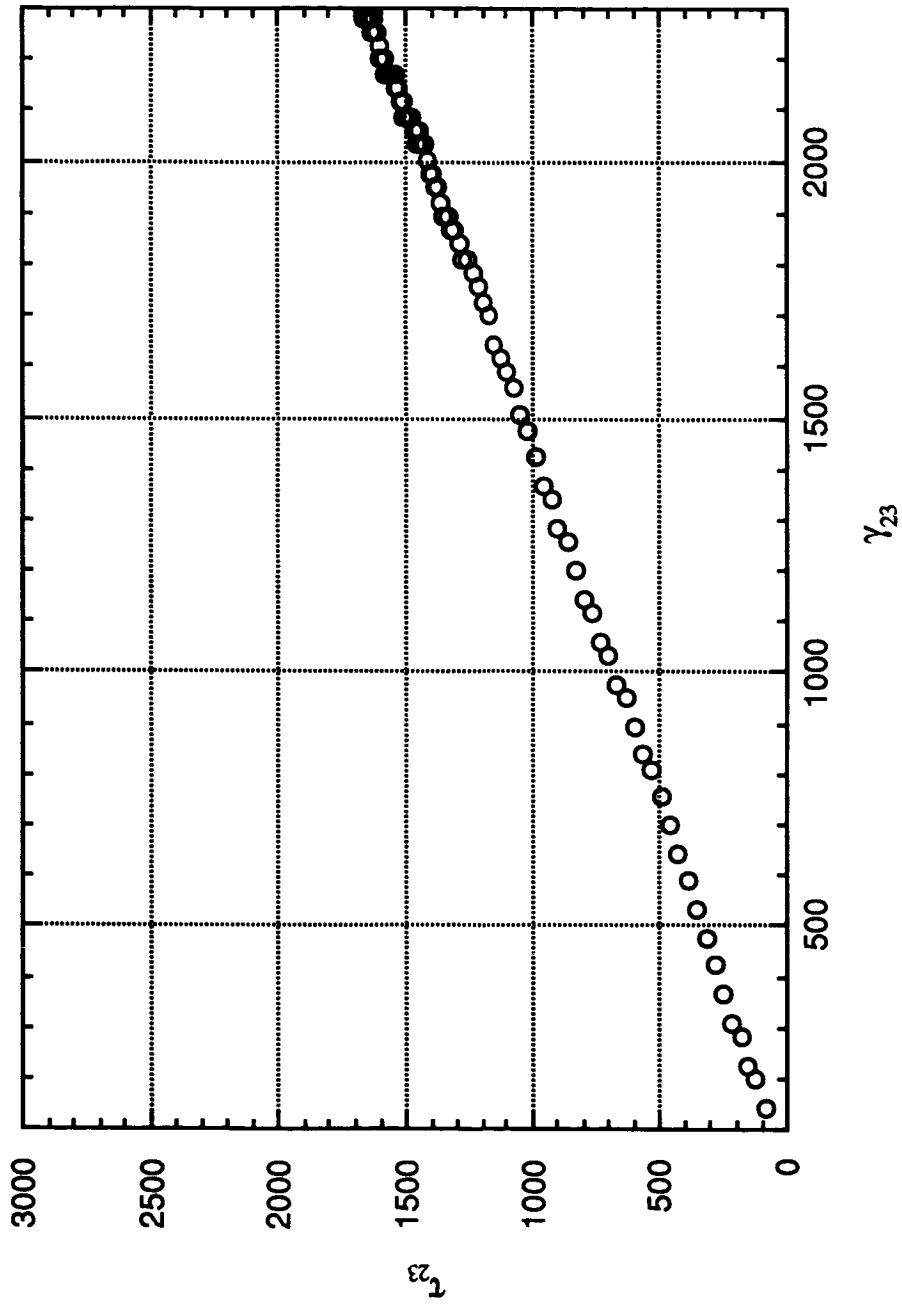

Figure 31 - Stress-strain curve for LS-3 composite using modified TTIS2 specimen configuration.